博士論文

Photocurrent and magneto-optical responses of topological insulators

(トポロジカル絶縁体における光電流及び磁気光学応答)

岡田　健

Abstract

Recent progress in condensed matter physics has uncovered topological aspects of fundamental importance for diverse phenomena in solids. For instance, topological properties in momentum space underlie quantum Hall and anomalous Hall effects as well as electric polarization in ferroelectrics, while those in real space play an essential role in magnetic materials hosting noncoplanar spin textures such as skyrmion lattices.

One of the most celebrated phenomena created by nontrivial topology in momentum space would be topological insulator (TI) realized in strongly spin–orbit-coupled materials, which hosts peculiar surface states in energy gap of bulk band structures. Those surface states are characterized with a massless Dirac dispersion endowed with spin–momentum locking, a property that spin orientation is uniquely determined by the momentum. Theorists have predicted unprecedented exotic phenomena in TI, including quantized magnetoelectric effect and Majorana fermions in proximity to superconducting phases. In parallel, an increasing amount of experimental efforts have discovered novel quantum transport of surface Dirac electrons such as quantum Hall effect, quantum anomalous Hall (QAH) effect and also their hybridized version. In addition they also revealed remarkable spintronic functionalities represented by highly-efficient spin–charge conversion. Thus TI has been gathering a growing interest from the viewpoints of both fundamental physics and practical applications.

In contrast to the novel static responses observed so far, electrodynamical responses of TI have not been well elucidated in experiments. This is partly because the response of surface Dirac electrons could be easily covered by the substantial response of bulk electrons in heavily-doped samples or at high-frequency regions.

In this thesis we explore optical properties of surface Dirac electron states using carrier-controllable high-quality samples and/or low-energy probes. Specifically we investigate two optical responses of TI, (i) photocurrent and (ii) magneto-optical responses.

For (i), we demonstrate a significantly large spin-polarized photocurrent spontaneously flowing on the TI surface upon irradiation of circularly-polarized light. The maximum value of the generation efficiency obtained in our experiment amounts up to those in semiconductor quantum wells well studied for decades. We find that the photocurrent, termed as circular photogalvanic (CPG) current, is dramatically enhanced by tuning the Fermi energy within the band gap of TI. The result strongly implies that scattering of surface Dirac electrons to bulk electronic states plays a crucial role in the microscopic process of CPG current generation.

For (ii), we observe quantization of magneto-optical Faraday and Kerr rotations in the QAH states on magnetic TI thin films. Remarkably, between those rotation angles hold a universal equation including solely the fine-structure constant $\alpha(= e^2/4\pi\epsilon_0\hbar c \sim 1/137)$, independent on material details such as dielectric constant or thickness of the film and substrate. In this aspect this can be regarded as a quantum phenomenon, along with quantum Hall or QAH effect and quantum flux in superconductors.

Altogether, we successfully reveal outstanding optical responses of surface Dirac electrons on TI, intriguing both in terms of fundamental physics and functionalities. We believe that our achievements will pave the way towards other novel optical phenomena predicted in TI as well as recently-discovered Weyl semimetals, regarded as the three-dimensional analogue of the surface Dirac electron states.

Contents

Chapter 1

Introduction

1.1 Topological insulator

1.1.1 Topology in crystals

The terminology of topology is originally a mathematical concept that classifies objects or space by their geometrical characteristics. For example, an orange and a donut are distinct in terms of topology—topologically distinct—, because the former has no hole, while the latter has one hole (Fig. 1.1(a)). This topological distinction ensures that they cannot be connected to each other by continuous transformation.

Theoretical progress in condensed matter physics for these decades have revealed that such a topological classification in mathematics can also be applied to electronic band structure in crystals through analogous discussions. In short, this is because an electronic band in a crystal shows its unique geometrical properties inherent in the Hilbert space spanned by N Bloch states represented by $|u_{n\mathbf{k}}\rangle$ (N: number of unit cells, n: band index, $\mathbf{k}$:crystal momentum). The geometrical property of a band structure can be characterized by an integer number termed as topological invariant, in a similar way to the number of holes mentioned above in the case of mathematical objects. Topological invariant is formulated with Berry connection $\mathbf{a}_n(\mathbf{k}) = -i \langle u_{n\mathbf{k}}|\nabla_{\mathbf{k}}|u_{n\mathbf{k}}\rangle$, which represents how much the phase in the Bloch state $|u_{n\mathbf{k}}\rangle$ evolves with an infinitesimal change in the momentum $\mathbf{k}$ [1].

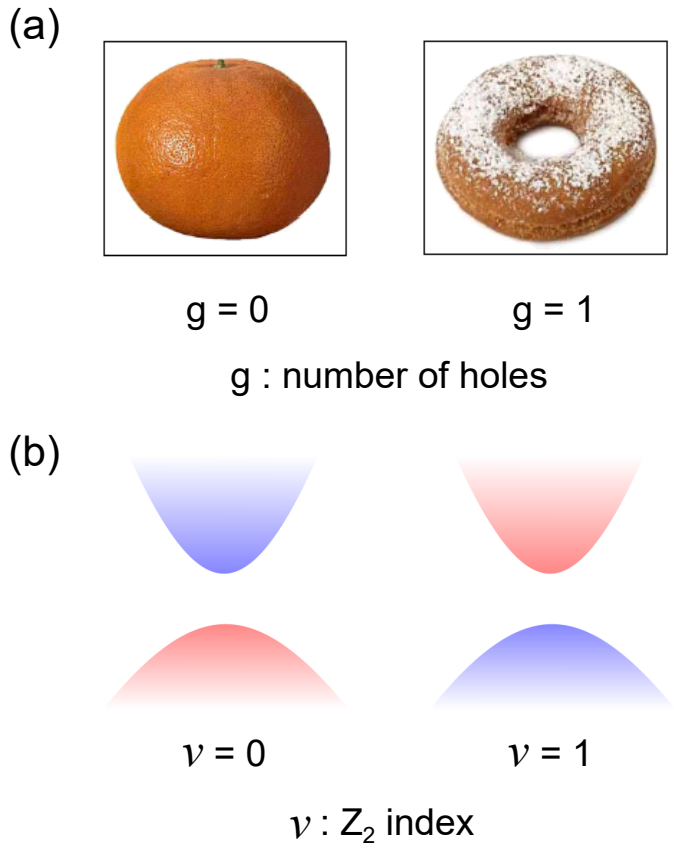

Figure 1.1: Schematic illustrations of (a) mathematical objects topologically distinguished with the number of holes g, and (b) crystal band insulators distinguished with a topological invariant called $\mathbb{Z}_2$ index ν, defined on electronic band structures under the preservation of time-reversal symmetry. The figures in (a) are adapted from Ref. [2].

The first example of topological invariant for crystals, the Chern number, was discovered in a seminal work by Thouless, Kohmoto, Nightingale and den Nijs (TKNN) [3]. The Chern number is defined on two-dimensional system and formulated for a band with index n as

$$\begin{aligned} \nu_n &= \int_{\mathrm{BZ}} \frac{d^2\mathbf{k}}{2\pi} \left(\frac{\partial a_{n,y}}{\partial k_x} - \frac{\partial a_{n,x}}{\partial k_y} \right) \\ &= \int_{\mathrm{BZ}} \frac{d^2\mathbf{k}}{2\pi} b_{n,z}. \end{aligned} \tag{1.1}$$

The value takes any integer and the system with nonzero Chern number is often called the Chern insulator. Here the Berry curvature $\mathbf{b}_n(\mathbf{k}) = \nabla_{\mathbf{k}} \times \mathbf{a}_n(\mathbf{k})$ is

defined.

The important point is that the Chern number is simply correlated with Hall conductance in the system as follows:

$$\sigma_{xy} = \frac{e^2}{h}\nu = \frac{e^2}{h}\sum_{n:\text{occupied}} \nu_n. \tag{1.2}$$

Thus, the Chern insulator just refers to quantum Hall effect and also quantum anomalous Hall (QAH) effect, both of which will be explained in more details in Sec. 1.3.

1.1.2 $\mathbb{Z}_2$ topological insulator

Recently, a new type of topological invariant, named $\mathbb{Z}_2$ topological invariant, has been discovered by Kane and Mele [4, 5]. The invariant was defined on band structures of two-dimensional [4,5], and later three-dimensional electronic systems [6, 7] under the presence of time-reversal symmetry. It takes only two values of 0 and 1. The former corresponds to trivial systems, while the latter corresponds to topologically-nontrivial systems, called $\mathbb{Z}_2$ topological insulator (TI), or merely TI. (For reviews of TI, see Refs. [2, 8]).

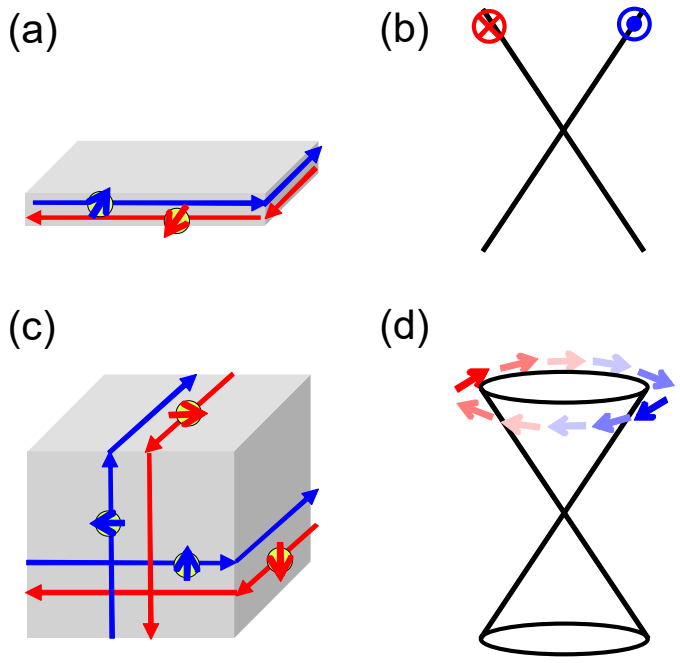

Figure 1.2: (a) Real-space schematic picture and (b) momentum-space energy dispersion of helical edge states on two-dimensional TI, i.e., quantum spin Hall insulator. (c), (d) corresponds to those of helical surface states on three-dimensional TI.

The prominent feature of TI is the emergence of helical edge or surface states characterized with a massless Dirac dispersion and spin–momentum locking, which states that the direction of spin is uniquely locked to the momentum. Note that those Dirac electrons are also called Weyl electrons, in a more strict sense. Those localized states necessarily appear at the boundary between TI and the vaccuum or any trivial material. For two-dimensional TI, in other words called quantum

spin Hall insulator, helical edge states appear around the edge of the system (Figs. 1.2(a) and 1.2(b)). The helical edge states exhibit quantization of longitudinal conduction because back-scattering from non-magnetic impurities is perfectly prohibited. For three-dimensional TI helical surface states appear on the surface of the system, with a Dirac-cone energy dispersion similar to graphene [9, 10] (Figs. 1.2(c) and 1.2(d)) (see also the Hamiltonian in Eq. (1.3)).

1.1.3 Topological insulator material

For realization of TI in real materials strong spin–orbit coupling plays an essential role. For inversion-symmetric crystals $\mathbb{Z}_2$ topological invariant coincides with the product of the parity eigen values of Bloch states for all the occupied bands and time-reversal-invariant momenta [11]. Accordingly, a common guiding principle is to search for materials associated with parity inversion between bulk valence and conduction bands, generated by spin–orbit coupling.

So far, an increasing number of materials have been identified as TIs both theoretically and experimentally. For two-dimensional TI materials, the first example of which is CdTe/HgTe/CdTe quantum well [12, 13], experimentalists have observed perfect conduction due to the helical nature of the edge states. For three-dimensional TI materials, often after theoretical predictions by density functional theory (DFT), helical surface states have been observed in angle-resolved photoemission spectroscopy (ARPES) and scanning tunneling microscopy (STM) [14]. In this thesis we work on three-dimensional TIs and below we refer to three-dimensional TI only as TI, unless stated.

Among TIs discovered so far the most well-known are layered chalcogenides Bi_2Se_3, Bi_2Te_3 and Sb_2Te_3. They are narrow-gap semiconductors with the band gap of 0.25–0.30 eV, originally famous for their high thermoelectric efficiency. Along c-axis in hexagonal representation a quintuple-layer (QL), block of Se–Bi–Se–Bi–Se in case of Bi_2Se_3, is sequentially stacked primarily by van-der-Waals interaction (Fig. 1.3(a)). Those materials are TIs because strong spin–orbit coupling induces interchange of energy levels with opposite parity across the chemical potential, as depicted in Fig. 1.3(b). Indeed, DFT [15] and ARPES [16–18] revealed that nontrivial surface states characterized with a Dirac-cone dispersion and spin–momentum locking exist at the Γ point between the bulk conduction and valence bands (Figs. 1.3(c) and 1.3(d)).

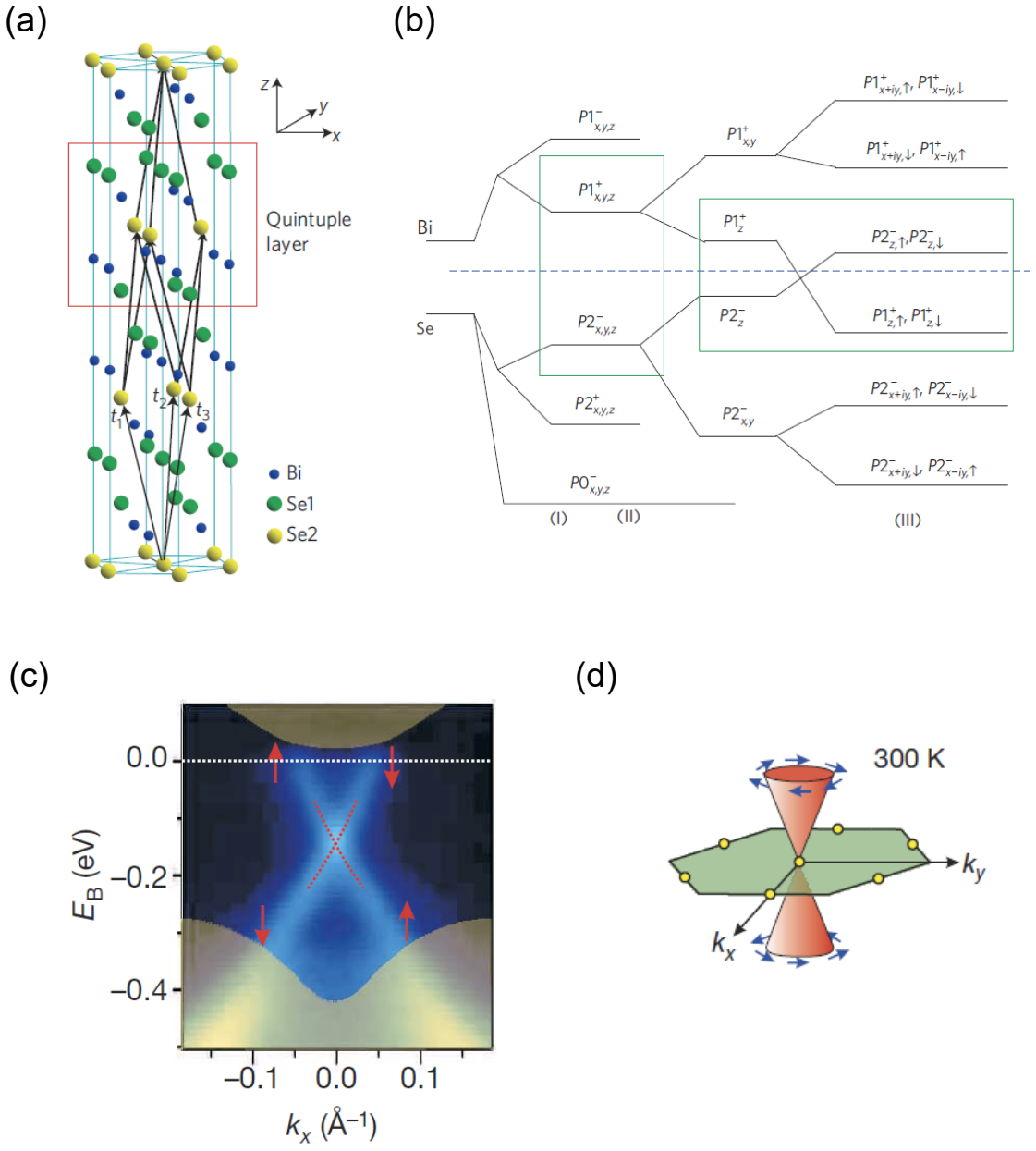

Figure 1.3: (a) Crystal structure of Bi_2Se_3. (b) Schematic diagram of the evolution of the atomic p_x, p_y and p_z orbitals of Bi and Se through introduction of chemical bonding, crystal-field splitting and spin–orbit coupling. (c) Energy dispersion of the helical surface states on Bi_2Se_3 obtained by ARPES. To lower the Fermi energy, only slight amount of Bi is substituted for Ca. (d) Schematic illustration of the surface Dirac states at the Γ point in the (111) surface Brillouin zone. The figures in (a) and (b) are adapted from Ref. [15] and those in (c) and (d) are taken from Ref. [17].

1.1.4 Thin films of topological insulator $(Bi_{1-x}Sb_x)_2Te_3$

Although Bi_2Se_3, Bi_2Te_3 and Sb_2Te_3 have been subject under intense study by transport and optical experiment so far [14], most of those experiments have been significantly affected by substantial number of bulk carriers. This is because in those compounds excessive electrons or holes are unintentionally doped by atomic defects and deficiencies, with the Fermi energy deep into the bulk conduction or valence band. Therefore, the response of surface states was often hard to discern, smeared out in that of bulk carriers.

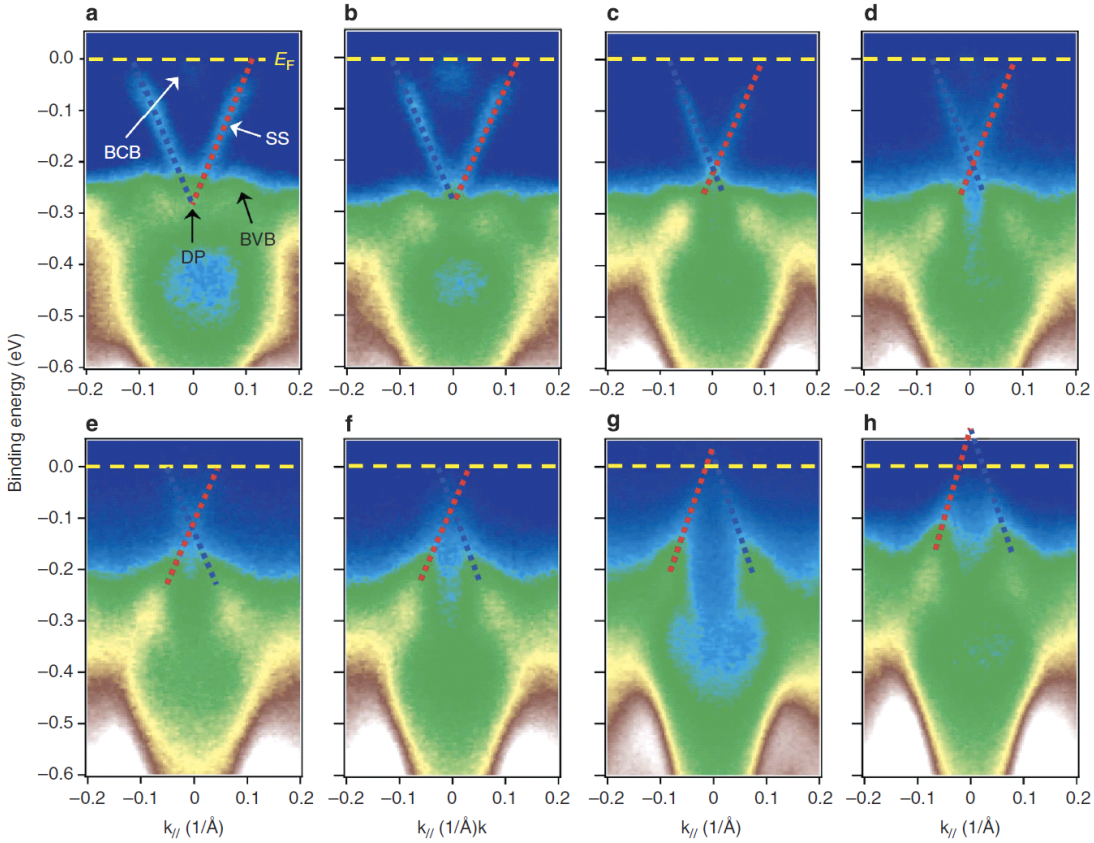

Figure 1.4: Energy dispersion of the surface Dirac states in $(Bi_{1-x}Sb_x)_2Te_3$ thin films, measured by ARPES. (a)–(h) correspond to samples of $x = 0$, 0.25, 0.62, 0.75, 0.88, 0.94, 0.96, and 1.0, respectively. The figure is adapted from Ref. [19].

Recently, it has been found that such a problem can be nicely avoided by using thin films of $(Bi_{1-x}Sb_x)_2Te_3$ [19]. Bi_2Te_3 and Sb_2Te_3 thin films grown by molecular beam epitaxy (MBE) show n- and p- type conduction, respectively. As a result, by

tuning Sb content x from 0.0 to 1.0 in $(Bi_{1-x}Sb_x)_2Te_3$ thin films the Fermi energy is smoothly shifted in a wide energy range from the bulk conduction band through the Dirac point in the surface states to the bulk valence band, as demonstrated in ARPES studies [19] (Fig. 1.4). This breakthrough has made it possible to capture the surface state response without being hindered by bulk carrier, leading to the striking observations of surface quantum transport such as quantum Hall effect [20], quantum anomalous Hall effect [21–26] and their hybridized version [27] as well as the accomplishments in this thesis.

1.2 Spin–charge conversion

A number of experiments and theories these years have discovered that surface Dirac electron states on TI show intriguing quantum phenomena with significant importance in the viewpoint of fundamental physics, as well as novel functionalities with potential application to future electronics. A representative example among the latter is the spin–charge conversion with remarkable efficiency [28–32], which would be harnessed for spintronics devices. On the other hand, among the former, one of the most celebrated ones is quantum anomalous Hall (QAH) effect [21–26], i.e., quantum Hall effect under zero magnetic field. The key ingredients for both effects are massless Dirac dispersion and spin–momentum locking in surface Dirac electron states.

In this and next sections we make a brief introduction to those two phenomena, which are closely related to the topics in Chaps. 3 and 4 in this thesis, respectively.

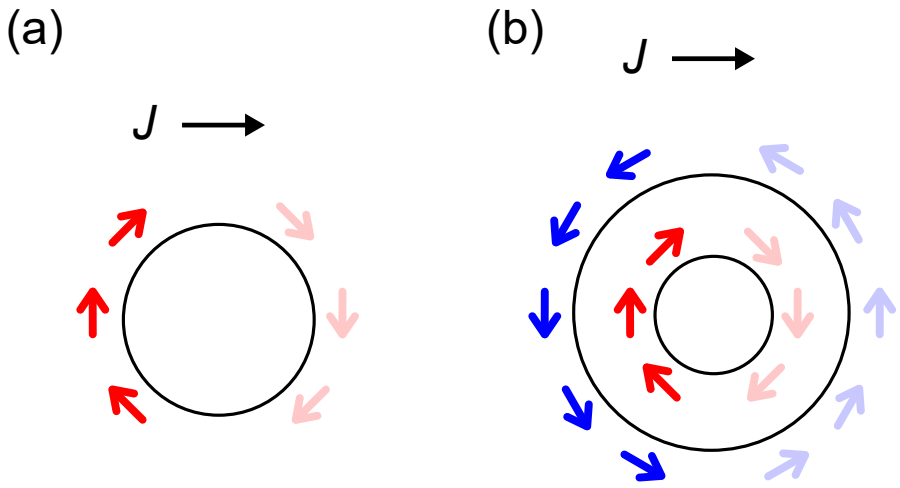

Figure 1.5: Schematic picture of spin polarization induced by flow of charge current in (a) the surface states of TI and (b) a two-dimensional Rashba system. J represents charge current. In (b) substantial cancellation occurs between the two bands with the opposite spin helicities.

In general, spin–momentum locking is a common feature of conduction electron systems with broken inversion-symmetry under the presence of spin–orbit couplings. Except for Dirac electron states on the surface of TI, those include two-

dimensional electron gas with Rashba- and Dresselhaus- type spin–orbit couplings originating from breaking of interface and bulk inversion symmetry, respectively. Such two-dimensional spin–orbit-coupled systems are often realized in semiconductor quantum wells or metal heterostructures.

When spin–momentum locking exists in energy bands, charge current is always accompanied with spin polarization and vice versa through antisymmetric carrier distribution in the momentum space, as schematically depicted for the cases of TI and Rashba systems in Figs. 1.5(a) and 1.5(b). This is often called Edelstein effect [33] and results in mutual conversion between spin and charge, termed as spin–charge conversion. Indeed, spin–charge conversion in those materials has been demonstrated in a number of experiments, by measuring spin-transfer torque produced by current injection [28] or detecting voltage generated by microwave-induced spin pumping [29].

As for the efficiency of spin–charge conversion TI has a notable advantage over conventional two-dimensional electron systems. Surface Dirac electron states on TI have a single spin-helical Fermi circle in the momentum space, while the latter possess double Fermi circles with the opposite spin helicities, leading to substantial cancellation of spin–charge conversion between the two bands (Figs. 1.5(a) and 1.5(b)). Indeed, a variety of experiments suggest that the efficiency is orders of magnitude higher in TI than that is in conventional two-dimensional electron systems, although it is still a controversial problem to quantitatively estimate how much higher [28, 30].

1.3 Quantum anomalous Hall effect

In this section we explain QAH effect after briefly reviewing quantum Hall effect.

Quantum Hall effect, together with fractional quantum Hall effect induced by electron correlation, is one of the central issues in the modern condensed matter physics due to their salient quantum-mechanical features. It was sensationally discovered in experiments by Klitzing, Dorda and Pepper in 1980 [34]. A few years later it was followed by several different kinds of theories of great importance, including thought experiment on a cylinder with flux penetration by Laughlin [35], introduction of edge states by Halperin [36] and proposal of topological properties by TKNN [3] as already mentioned in Sec. 1.1.1. Quantum Hall effect occurs through the formation of Landau levels when strong magnetic field is applied perpendicular to a clean two-dimensional electron system. Then Hall conductance is quantized at an integer multiple of conductance quantum as $\sigma_{xy} = \frac{e^2}{h}\nu$. Here ν coincides with the number of the filled Landau levels, named filling factors and depends on the strength of magnetic field and chemical potential. So far, it has been observed in semiconductor quantum wells such as GaAs/AlGaAs [34], graphene [9, 10] and lately the surface states of TI [20, 37].

On the other hand, theorists have proposed several ways of realizing Hall conductance quantization, in other words, the Chern insulator without external magnetic field [38, 39]. Moreover, during this century the understanding of anomalous Hall effect in ferromagnetic metals has been renewed by shedding light on its topological aspects, namely nontrivial Berry curvatures generated by magnetization and spin–orbit coupling [40].

In this context, quantization of anomalous Hall effect, termed as quantum anomalous Hall (QAH) effect, has been predicted to occur in the surface states of TI in the presence of magnetic moment normal to the TI surface [41, 42]. The Dirac surface states coupled with the perpendicular magnetization are most simply described by the following Hamiltonian:

$$H(\mathbf{k}) = \hbar v(\pm k_y\sigma_x \mp k_x\sigma_y) + \frac{1}{2}Jmg\mu_{\mathrm{B}}\sigma_z. \tag{1.3}$$

Here σ_μ ($\mu = x, y$ and z) represents a Pauli matrix for spin degrees of freedom

and v denotes the velocity of the massless Dirac electrons, g the g-factor, J the exchange interaction strength, m the magnetization. Note that $\pm$ corresponds to the top and bottom surface on the TI slab, signifying the opposite helicities. The energy dispersions are derived from Eq. (1.3) as

$$E(\mathbf{k}) = \pm\hbar v\sqrt{k_x^2 + k_y^2 + \Delta^2}, \tag{1.4}$$

where Δ is defined as $\Delta = Jmg\mu_{\mathrm{B}}/2\hbar v$. This indicates that an energy gap with the size of 2Δ, called a mass gap, is introduced at the Dirac point by the magnetic moment (see Figs. 1.6).

The remarkable point is that this gap opening provides the divergent Berry curvature $b_z(\mathbf{k})$ at the Dirac point. As a result, in the case that the Fermi energy is located within the mass gap, the Hall conductance, derived from Eqs. (1.1) and (1.2), is quantized at e^2/h in total, which is contributed by the top and bottom surface states by halves.

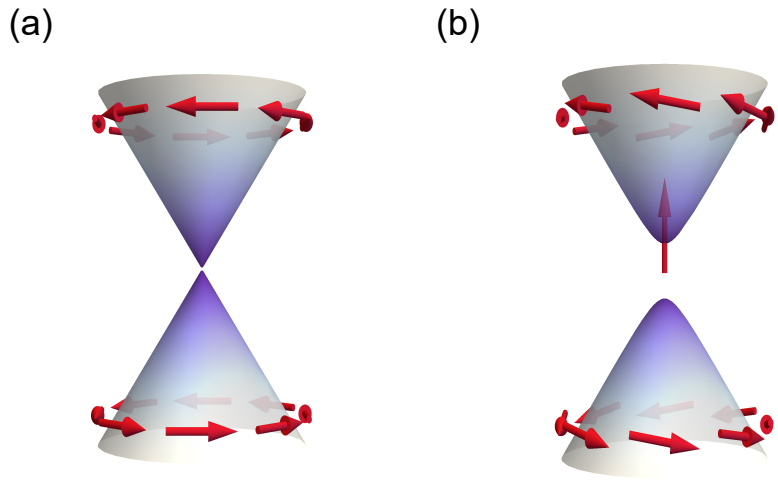

Figure 1.6: Schematic illustrations of (a) massless Dirac dispersion of the TI surface states and (b) massive ones induced by the magnetic moment perpendicular to the surface. Red arrows denote spins locked to the corresponding momenta.

According to the predictions, QAH effect has been experimentally observed on $(Bi_{1-x}Sb_x)_2Te_3$ thin films doped with Cr or V as impurities at a few tens of millikelvin [21–25]. More recently, it has been found out that by doping Cr in a spatially-modulated way in $(Bi_{1-x}Sb_x)_2Te_3$ thin film QAH effect has been

stabilized at orders of magnitude higher temperature, namely a few Kelvin [26] (For the details see Sec. 4.2). This heterostructure engineering allows various experimental investigations of QAH effect like optical measurements as we employ in Chap. 4.

1.4 Motivation and purpose of the thesis

As explained so far, increasing efforts of previous studies have uncovered intriguing static responses of TI like spintronic functionalities and quantum transports. On the other hand, electromagnetic responses of surface Dirac electron states still remain elusive. There exist several optical studies on photocurrent [43–45] and cyclotron resonances [46–52] in TI, but most of them are substantially affected by large response from sizable number of bulk carrier, which often makes unclear or even masks the smaller responses of the surface states. This is mainly due to unintentional carrier-doping by defects in samples (see Sec. 1.1.4) or photon energy exceeding the band gaps.

In this context the goal of this theses is to experimentally elucidate unexplored novel optical phenomena in TI by extracting the response of the surface Dirac electron states in a maximum degree with using carrier-tuned samples and low-energy probes. Towards this goal we focus on two outstanding optical phenomena appearing in TI; (i) circular photogalvanic (CPG) effect (Chap. 3) and (ii) quantized magneto-optical effect on QAH states (Chap. 4).

Actually, those two phenomena can be regarded as the optical counterparts of spin–charge conversion and QAH effect, introduced in Secs. 1.2 and 1.3, respectively. The former is a kind of photovoltaic effect, where spin-polarized photocurrent spontaneously flows by irradiation of circularly-polarized light on spin–momentum-locked systems such as TI surface states. It can be considered as spin–charge conversion in a broad sense, because charge current is driven by effective spin injection via circular polarization of photon. The latter is the quantization of magneto-optical Faraday and Kerr rotation angles without magnetic field, which has been predicted to occur on TI exhibiting the QAH effect. This corresponds to an optical version of QAH effect, because it stems from the quantization of the Hall conductance at finite frequency. The details of those phenomena will be described in Secs. 3.1 and 4.1, respectively.

The organization of this theses is as follows. In Chap. 2 we make detailed explanations of the samples and optical measurements employed in this theses. In Chap. 3 we demonstrate an efficient generation of CPG current on TI, through

precise tuning of the Fermi energy. We discuss the strong correlation between the CPG current and the Fermi energy in terms of scattering mechanisms. In Chap. 4 we present an optical quantum phenomenon on TI, characterized with Faraday and Kerr rotation angles defined by the fine-structure constant α ($= e^2/4\pi\epsilon_0\hbar c \sim 1/137$). We confirm that those rotation angles are quantitatively consistent with QAH effect in the d.c. limit. Finally, in Chap. 5 we state the summary of this theses and the future perspectives derived from the results.

Chapter 2

Experimental methods

2.1 Sample preparation and characterization

In this thesis we perform experiments on topological insulator (TI) thin films fabricated by molecular beam epitaxy (MBE). We prepare $(Bi_{1-x}Sb_x)_2Te_3$ (BST) films with a MBE apparatus in RIKEN and are provided with Cr-doped BST (CBST) films grown in RIKEN by Mr. M. Mogi. Both sample are 8-nm-thick and grown on both-side-polished InP(111) substrates. To prevent film degradation all the samples for the measurement are covered with AlO_x layers ($\sim$ 10 nm) deposited by the atom layer deposition (ALD) at room temperature, just after taking out the samples from the MBE chamber.

For the growth of BST films we follow the procedure in Ref. [53]. Before setting a substrate in the preparation chamber of the MBE apparatus, we eliminate possible contaminants on the substrate by nitrogen gas blow. In the vacuum-sealed growth chamber we anneal the substrate for the better surface morphology by heating it up to 340 °C and then cool it down to the growth temperature, 200 °C. Meanwhile, we adjusted the temperature of each Knudsen cell (K-cell) so that the flux ratio between Bi, Sb and Te should be $x : 1 - x : 10$. Note that due to high vapor pressure of Te, we provide excessive Te flux to prevent Te evaporation from the film surface during the growth. We start the deposition as we open the shutters of the K-cells. After the growth we close only the shutters of the Bi and Sb cells, keeping Te flux supplied until the temperature is lowered down to 180 °C.

This is very important to suppress Te deficiency near the film surface, which we confirmed would introduce extra bulk carrier. For the CBST films the growth process is basically the same as that of the BST films mentioned above, except the post-annealing procedure after the growth.

We characterize the structural properties of thin films without AlO_x capping layers by X-ray diffraction (XRD) and atomic force microscopy (AFM). Figs. 2.1(a) and 2.1(b) show a representative θ–2θ XRD pattern around the $(0, 0, 0, 15)$ peak and an AFM image of a BST film, respectively. The XRD pattern shows Laue fringe around the peak, indicating high layer coherence along the film growth direction. In the AFM image step-and-terrace structures are observed, with the height of each step around 1 nm, corresponding to one quintuple-layer of the BST. This proves atomic-level flatness of the surface.

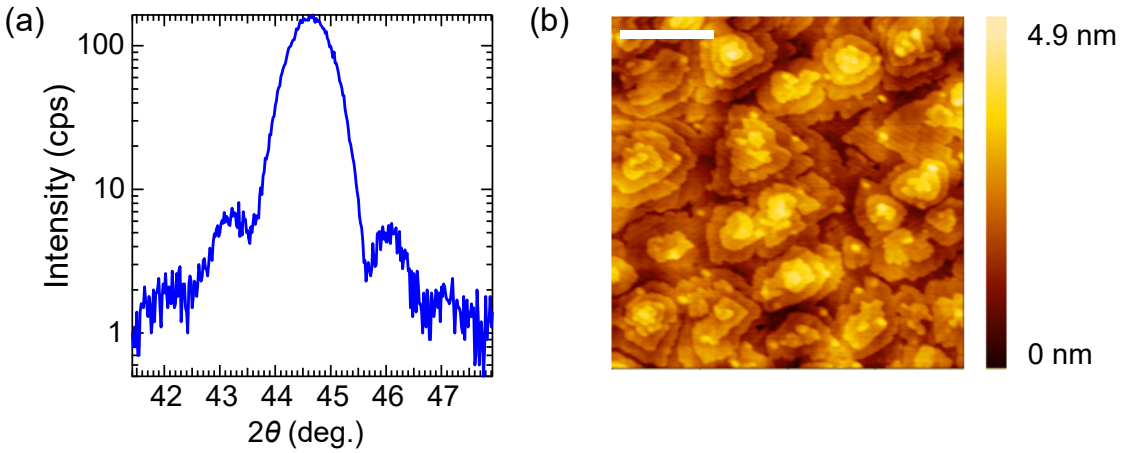

Figure 2.1: (a) A typical θ–2θ XRD pattern and (b) AFM image of a BST film. The white bar in (b) corresponds to 500 nm.

2.2 Transport measurement

For the transport measurement we attach gold wires to samples with silver paste as electrodes. Then we measure longitudinal and Hall resistance, R_{xx} and R_{yx} with a standard four-probe method by using Physical Property Measurement System (PPMS) of Quantum Design Inc. Here temperature is varied from 300 K to 2 K and down to 1.5 K with a He3 option attached to PPMS, and magnetic field is applied up to 9 T perpendicular to the film.

We measure BST films covered with AlO_x layers and FET devices fabricated from CBST films. In the FET devices 30-nm-thick AlO_x films deposited by ALD are used as gate insulating layers.

2.3 Photocurrent measurement

We measure photocurrent in BST films. For the photocurrent detection we use silver paste as electrodes. Figure 2.2 schematically represents the optical setup for photocurrent measurement. A c.w. Nd:YAG laser (1.17 eV) is irradiated on a sample, modulated by an optical chopper at 397 Hz. The photon polarization is controlled by rotating a $\lambda/4$ plate. We carefully locate the laser spot with the diameter around 1 mm almost in the middle between the electrodes on the sample separated by ~ 3 mm, to avoid illuminating the electrodes. For the front illumination the light is incident on the AlO_x capping layer of the sample, while for the back illumination it is incident on the substrate of the sample.

The short-circuit zero-bias photocurrent is measured by a lock-in amplifier with the reference signal from the chopper. Before measuring the sample, we measure the signal of a photo diode illuminated by the laser and set the obtained phase to zero. This calibration allows us to determine the current direction. Note that we can neglect photocurrent contribution from the InP substrate because it is transparent for the incident laser; the band gap of InP (1.34 eV) is larger than the photon energy.

All the photocurrent measurements were performed at room temperature.

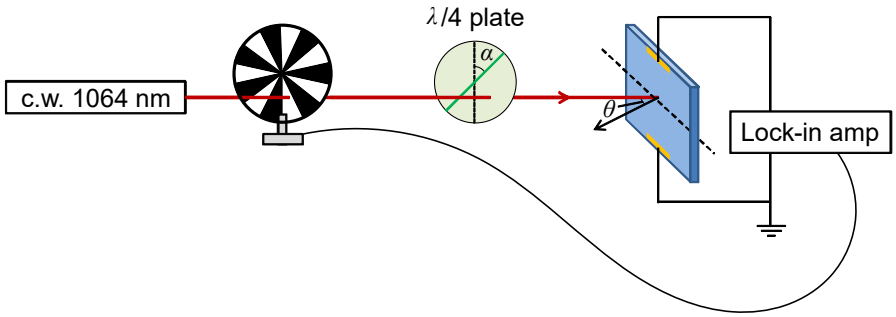

Figure 2.2: Schematic diagram of the photocurrent measurement setup.

2.4 Terahertz magneto-optical measurement

We perform magneto-optical measurement on CBST films in terahertz (THz) region. For THz optics we employ THz time-domain spectroscopy (THz-TDS).

Figure 2.3 shows a schematic diagram of the optical setup. In the THz-TDS, laser pulses with a duration of 100 fs from a mode-locked Ti:sapphire laser are split into two paths to generate and detect THz pulses. The laser is modulated by an optical chopper at 3 Hz. THz pulses incident on the sample are generated by transient photocurrent in a bow-tie shaped antenna triggered by irradiation of the pump laser. On the other hand, THz pulses trasmitted through the sample illuminates a dipole antenna and drives photocarrier generated by the probe laser, which is detected as an electric current by a lock-in amplifier with the reference signal from the optical chopper.

For magneto-optical measurement we prepare three wire-grid polarizers for polarization of THz light. In general, two polarizers are sufficient for magneto-optical experiment, but we use three to save time and effort of rotating the polarizer. One polarizer is located before the sample to polarize the incident light along x direction. Here we define x-, y- and z- axes as shown in Fig. 2.3. The other two are located after the sample, working as analyzers. The first analyzer A1, located just after the sample, permits the transmittance of light with electric field projected onto $y = x$ direction. The second analyzer A2, located after A1, allows transmittance of light only with y-component of electric field (E_y). When we measure x-component of electric field of the transmitted light (E_x), we use both A1 and A2. Note that the signal of E_x is reduced by half. When we measure y-component of the electric field (E_y), we only use A2, taking A1 away (Crossed-Nicole geometry). By employing those three polarizers, we can measure E_x and E_y through insertion and removal of the analyzer A1, instead of rotating a polarizer.

In most of the experiments we measure $E_x(t)$ and $E_y(t)$ at $B = 0$ T. Since $E_y(t)$ is very small, about two orders of magnitude smaller than $E_x(t)$, the background signal is significant. Therefore we deduce $E_y(t)$ through antisymmetrization, calculating the difference between the signals with magnetization for $\pm z$ directions after training at $\pm$ 1 T: $E_y(t) = (E_y^{+M}(t) - E_y^{-M}(t))/2$. For finite magnetic field,

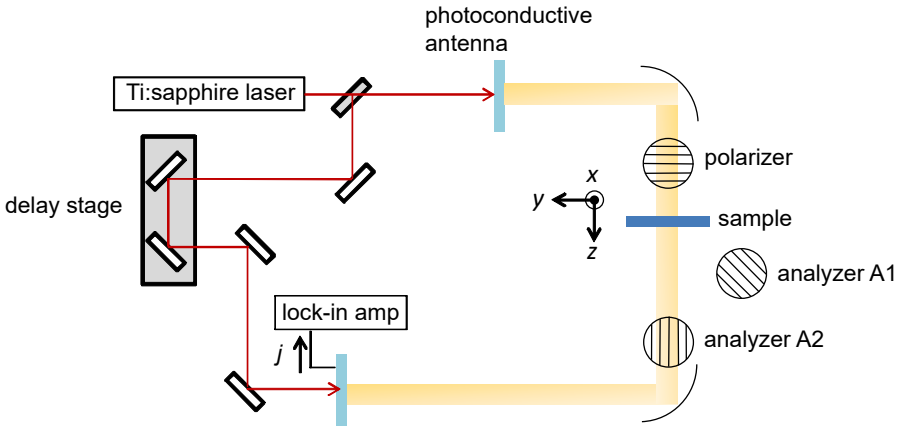

Figure 2.3: Schematic diagram of the optical setup of the THz magneto-optics. The incident THz light is polarized along $x-$axis. In measuring E_y for transmitted light we only use the analyzer named A2 as depicted above. On the other hand, in measuring E_x, we insert A1 between the sample and A2 then we obtain the half of the signal.

we derive $E_y(t)$ by the similar antisymmetrization: $E_y(t) = (E_y^{+1\mathrm{T}}(t) - E_y^{-1\mathrm{T}}(t))/2$. Note that we confirmed that Faraday rotation in InP substrate is negligibly small, indiscernible within the sensitivity of our equipment (< 10 μrad T^{-1}).

After calculating the Fourier transforms of $E_x(t)$ and $E_y(t)$, denoted by $E_x(\omega)$ and $E_y(\omega)$, we derive the magneto-optical rotation spectra $\theta(\omega)$ and ellipticity spectra $\eta(\omega)$ by the following formula:

$$\frac{E_y(\omega)}{E_x(\omega)} = \frac{\sin\theta(\omega) + i\eta(\omega)\cos\theta(\omega)}{\cos\theta(\omega) - i\eta(\omega)\sin\theta(\omega)}. \tag{2.1}$$

Note that for small $\theta(\omega)$ and $\eta(\omega)$ Eq. (2.1) is simply written down as

$$\frac{E_y(\omega)}{E_x(\omega)} \sim \theta(\omega) + i\eta(\omega). \tag{2.2}$$

We also derive the longitudinal optical conductance $\sigma_{xx}(\omega)$ from the following formula:

$$t(\omega) = \frac{1 + n_\mathrm{s}}{1 + n_\mathrm{s} + Z_0\sigma_{xx}(\omega)}, \tag{2.3}$$

where $t(\omega)$ is the Fourier transform of the complex transmittance, Z_0 is the impedance of free space (377 Ω) and n_s the refractive index of the InP substrate. Here we deduce the complex transmittance dividing $E_x(t)$ for the sample by that for the substrate.

Chapter 3

Enhanced circular photogalvanic effect via Fermi energy tuning

3.1 Introduction

In this Chapter we show an efficient generation of spin-polarized photocurrent, in other words circular photogalvanic (CPG) current driven by surface Dirac electrons on topological insulator (TI) by means of accurate control of the Fermi energy (E_{F}). In this section we make a brief description of the CPG effect and introduce related studies on TI.

3.1.1 Circular photogalvanic effect

As mentioned in Sec. 1.2 spin–charge conversion phenomena commonly appear in spin–momentum-locked systems, namely, spin–orbit-coupled electronic systems without inversion symmetry, such as TI surface states and semiconductor quantum wells. On those systems it has been also known that spin-polarized photocurrent is generated by circularly-polarized light, termed as circular photogalvanic effect. Roughly speaking, this photomagnetic effect is an extended version of spin–charge conversion phenomena, due to effective spin pumping through transfer of photon angular momentum to electrons.

A hallmark of the CPG effect is reversal of current direction (and consequently the spin orientation) by flip of the photon helicity, which readily finds applications

in opto-spintronics. Such CPG effects have been well studied in semiconductor quantum wells, e.g., GaAs/AlGaAs [54], and more recently observed in other systems with stronger spin–orbit coupling, including TIs [43–45], bulk Rashba semiconductors [55], and transition metal dichalcogenides [56, 57].

The essential mechanism of the photocurrent driven by circularly-polarized light is asymmetric transient carrier population in the momentum space imposed by the optical selection rules [54, 58]:

$$\Delta m_j = \begin{cases} +1 & (\sigma_+) \quad (3.1a) \\ -1 & (\sigma_-). \quad (3.1b) \end{cases}$$

Here m_j represents secondary quantum number of total angular momentum j and $\sigma_{+(-)}$ stands for right(left)-handed circular polarization. Figures 3.1(a) and 3.1(b) schematically represent typical asymmetric excitations by circularly-polarized light responsible for CPG effect in semiconductor quantum wells.

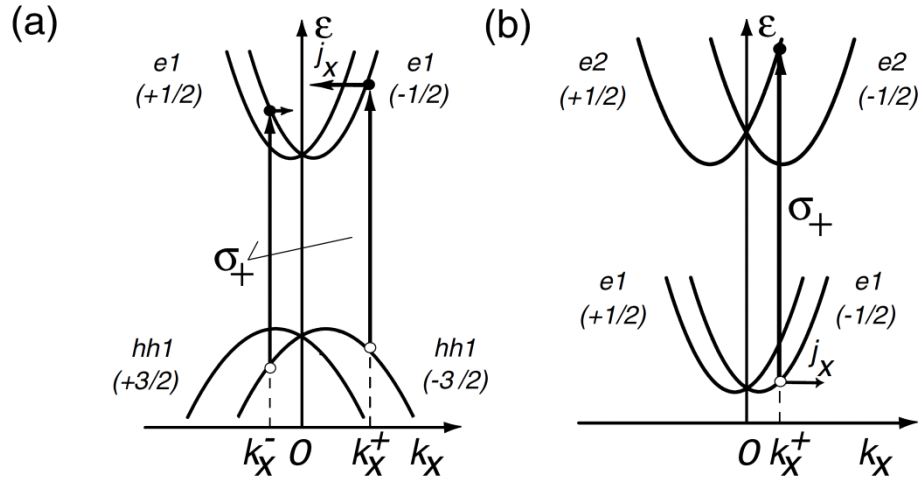

Figure 3.1: Schematic illustrations of asymmetric excitations in the momentum space by circularly-polarized light in semiconductor quantum wells. Upon irradiation of right-handed circularly-polarized light (σ_+) optical transitions occur (a) from valence band $hh1$ ($m_j = -3/2$) to conduction band $e1(m_j = -1/2)$ or (b) from one conduction subband ($m_j = -1/2$) to another ($m_j = 1/2$). The figures are adapted and modified from Ref. [54].

As a result of those helicity-dependent photo-excitations, CPG current is phenomenologically expressed by the following formula [54]:

$$j_\mu = E^2 P_{\mathrm{circ}} \sum_\nu \gamma_{\mu\nu} e_\nu, \tag{3.2}$$

where j_μ denotes the μ-th component of CPG current, $\mathbf{e}$ the unit vector representing light propagation direction, E the electric field of light. P_{circ} is the light helicity and equals ± 1 for $\sigma_\pm$, respectively. It is described as $P_{\mathrm{circ}} = \sin\phi$ by using the phase difference in two orthogonal components of electric field of light, ϕ.

3.1.2 Previous studies on topological insulator

TI is expected to be a promising candidate as an efficient generator of CPG current. This is because, as in the case of spin–charge conversion already mentioned in Sec. 1.2, CPG current is naturally expected to be larger in TI than in conventional two-dimensional electron systems, due to the absence of the compensation between the two Fermi surfaces with the opposite spin helicities (see Fig. 1.5). So far, several works have reported observations of CPG effect on TI, but only on Bi_2Se_3 [43–45], with E_{F} buried deep into the bulk conduction band (see also Sec. 1.1.4). Therefore, it is important to find optimal chemical potential to maximally draw out the CPG current inherent in the surface Dirac electrons. In this Chapter we aim to optimize CPG current in TI through the careful investigation of its E_{F}-dependence by using the carrier-controllable $(Bi_{1-x}Sb_x)_2Te_3$ (BST) thin films.

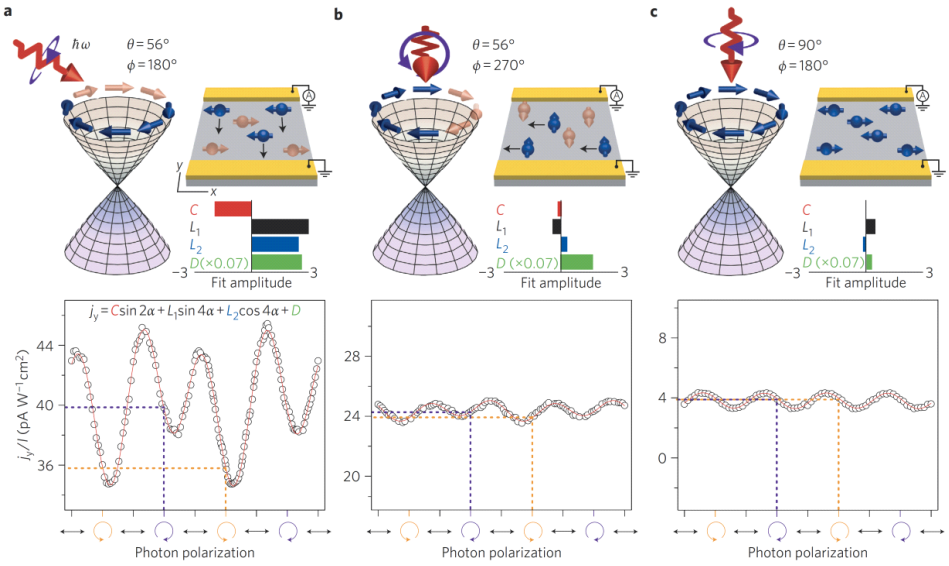

Figure 3.2: CPG effect observed on Bi_2Se_3 thin flakes [43].

3.2 Circular photogalvanic effect on a $(Bi, Sb)_2Te_3$ thin film

In this section we show the characteristics of the CPG effect that we observed in a BST film with E_F tuned within the bulk band gap and just above the Dirac point (DP) ($x = 0.80$). For the relation between E_F and x, see Sec. 3.3.1.

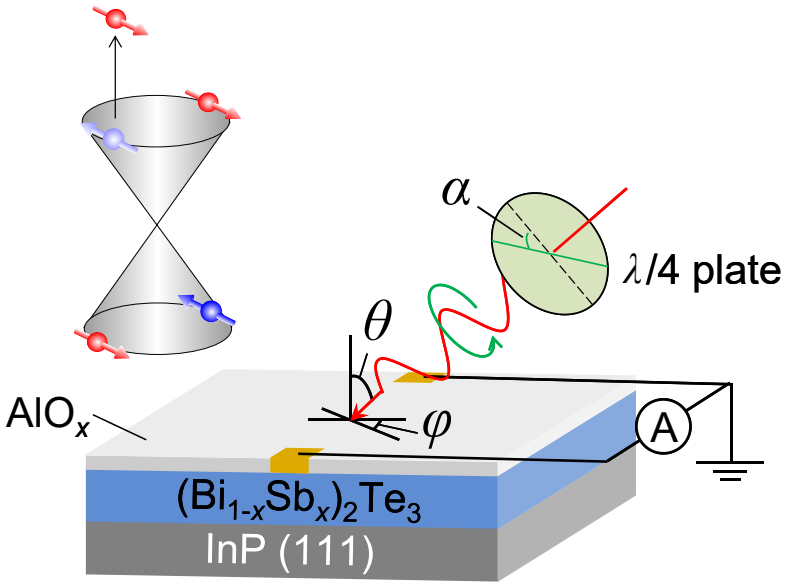

Figure 3.3: Schematic illustration of the photocurrent measurement. The laser is irradiated on the sample at the incident angle θ and azimuthal angle φ.

The experimental setup for the photocurrent measurement is schematically illustrated in Fig. 3.3. The incident angle θ and azimuthal angle φ are defined for the laser path as shown in Fig. 3.3. The photon energy of the laser is 1.17 eV, much larger than the band gap of BST (0.25 eV). For more details of the method, see Sec. 2.3.

Figure 3.4 displays the light-polarization dependence of the photocurrent for $\theta = 45$ deg. and $\varphi = 0$ deg. Here we control the light helicity P_{circ} (see Eq. (3.2)) by changing the rotation angle α of the $\lambda/4$ plate. The distinct difference in the photocurrent for the oppositely-handed circular polarizations definitely shows an emergence of the CPG effect (Fig. 3.4). This indicates that surface Dirac electrons are driven by photon helicity, through asymmetric excitations from the occupied

surface (bulk) states to the unoccupied bulk (surface) states. Note that since the band structures of bulk BST are spin-degenerate due to the presence of inversion symmetry, contributions from bulk-to-bulk transitions are generally cancelled out.

As in the previous report on Bi_2Se_3 thin flakes [43], the measured photocurrent is well fitted by

$$J = C \sin 2\alpha + L_1 \sin 4\alpha + L_2 \cos 4\alpha + D. \tag{3.3}$$

Here α denotes the angle of the quarter-wave plate. The first π-periodic term represents the CPG effect and the magnitude C is defined as the CPG current. On the other hand, the other $\pi/2$-periodic and constant terms are independent on photon helicity. We ascribe the D component to the thermally-induced current driven by the temperature gradient and the L_2 component to the modulation of D by the Fresnel factor [43]. The L_1 component is not unambiguously identified yet; this may include linear photogalvanic effect caused by asymmetric scattering [59].

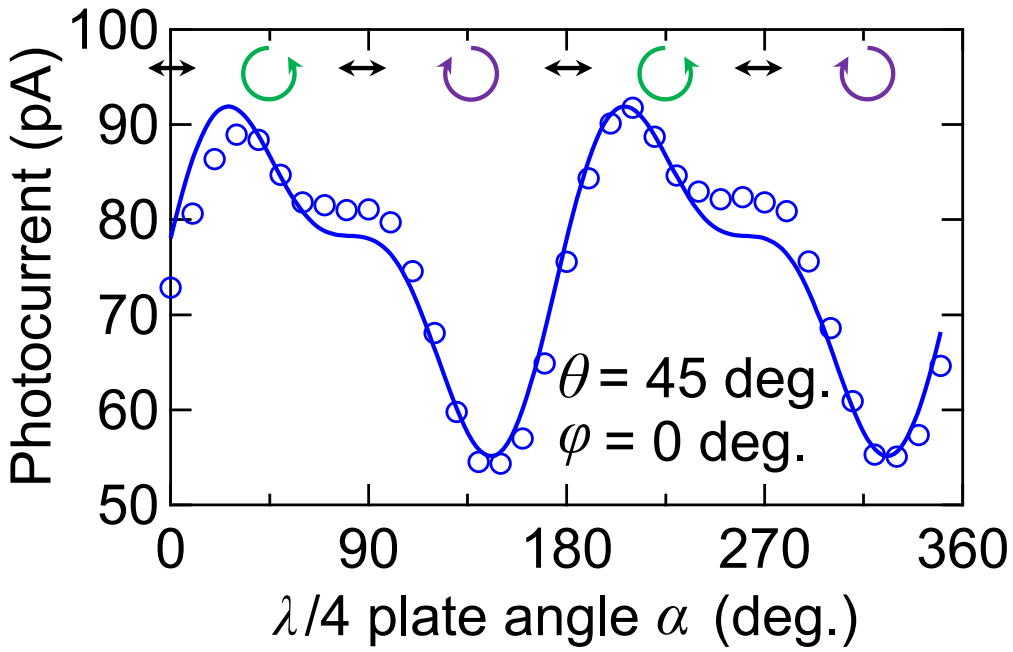

Figure 3.4: Light-polarization dependence of the photocurrent for $\theta = 45$ deg. and $\varphi = 0$ deg. in the BST ($x = 0.80$) film. The solid line represents fitting by Eq. (3.3).

Through similar measurements for various geometries of light irradiation, we find that the CPG current (C) shows a cosine-like function of the azimuthal angle φ at the incident angle $\theta = 45$ deg. (Fig. 3.5(a)) and vanishes at the normal incidence ($\theta = 0$ deg.) (see Fig. 3.11). Apparently, this is consistent with the helical spin texture of the surface Dirac cone. We also confirmed that as indicated by Eq. (3.2) the CPG current varies linearly with the light intensity (Fig. 3.5(b)).

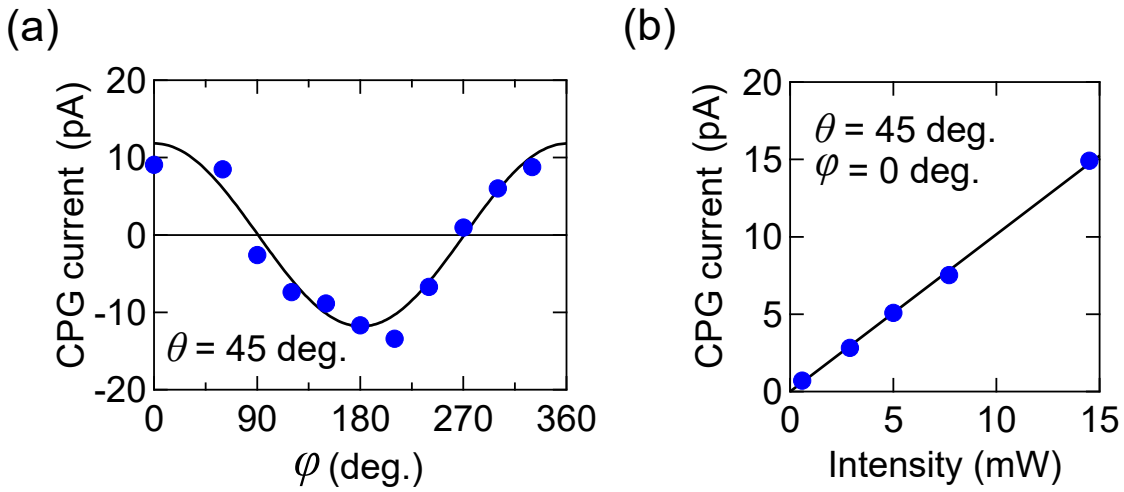

Figure 3.5: (a) Azimuthal angle dependence of the CPG current at $\theta = 45$ deg. The solid line represents a cosine function. (b) Laser intensity dependence of the CPG current at $\theta = 45$ deg. and $\varphi = 0$ deg.

3.3 Evolution of circular photogalvanic effect by tuning Fermi energy

3.3.1 Results

To understand how the CPG current changes by tuning the position of E_F, we compare the photocurrents for BST thin films with the Sb content x varied from 0.0 to 1.0; the results are summarized in Fig. 3.6.

First, we explain the variation of the transport properties, which well reproduced the previous study [19]. The transport properties shown in Figs. 3.6(a) and 3.6(b) indicate that E_F is systematically modified across the DP. We note that three samples ($x = 0.82$, 0.86 and 0.88, represented with dashed lines in Figs. 3.6) were fabricated during another experimental run, and seem to slightly deviate from the overall trend in R_{xx} (Fig. 3.6(a)), due probably to small change in the MBE chamber environment. However, these fluctuations do not affect our conclusions as we see below. For Bi_2Te_3 ($x = 0.0$), since R_{xx} shows metallic behavior and R_{yx} is negative, E_F lies in the conduction band. With increasing x from 0.0 to 0.84, R_{xx} and the absolute value of the Hall coefficient ($|R_H| = |R_{yx}|/B$) increases, which means the downward shift of E_F towards the DP. As x increases from 0.84 to 0.86, R_{yx} switches from negative to positive, signifying the change of the carrier type from electron to hole with E_F crossing the DP. Note that samples of $x = 0.84$–0.88 show smaller $|R_{yx}|$ (Fig. 3.6(b)) and seem to have larger carrier densities (Fig. 3.7) than those in the adjacent samples ($x = 0.82$ and 0.90). However, this is probably due to electron-hole puddles commonly observed when E_F is very close to the DP [20]. In Sb_2Te_3 ($x = 1.0$), a metallic behavior is recovered in R_{xx}, and therefore E_F is located in the bulk valence band. Such a systematic variation of the transport properties ensures the precise tuning of E_F with the Sb content x [19]. As we combine those transport properties with band parameters from previous theoretical and experimental works [19, 53, 60, 61], we find that E_F lies within the bulk band gap for $x = 0.80$–0.88.

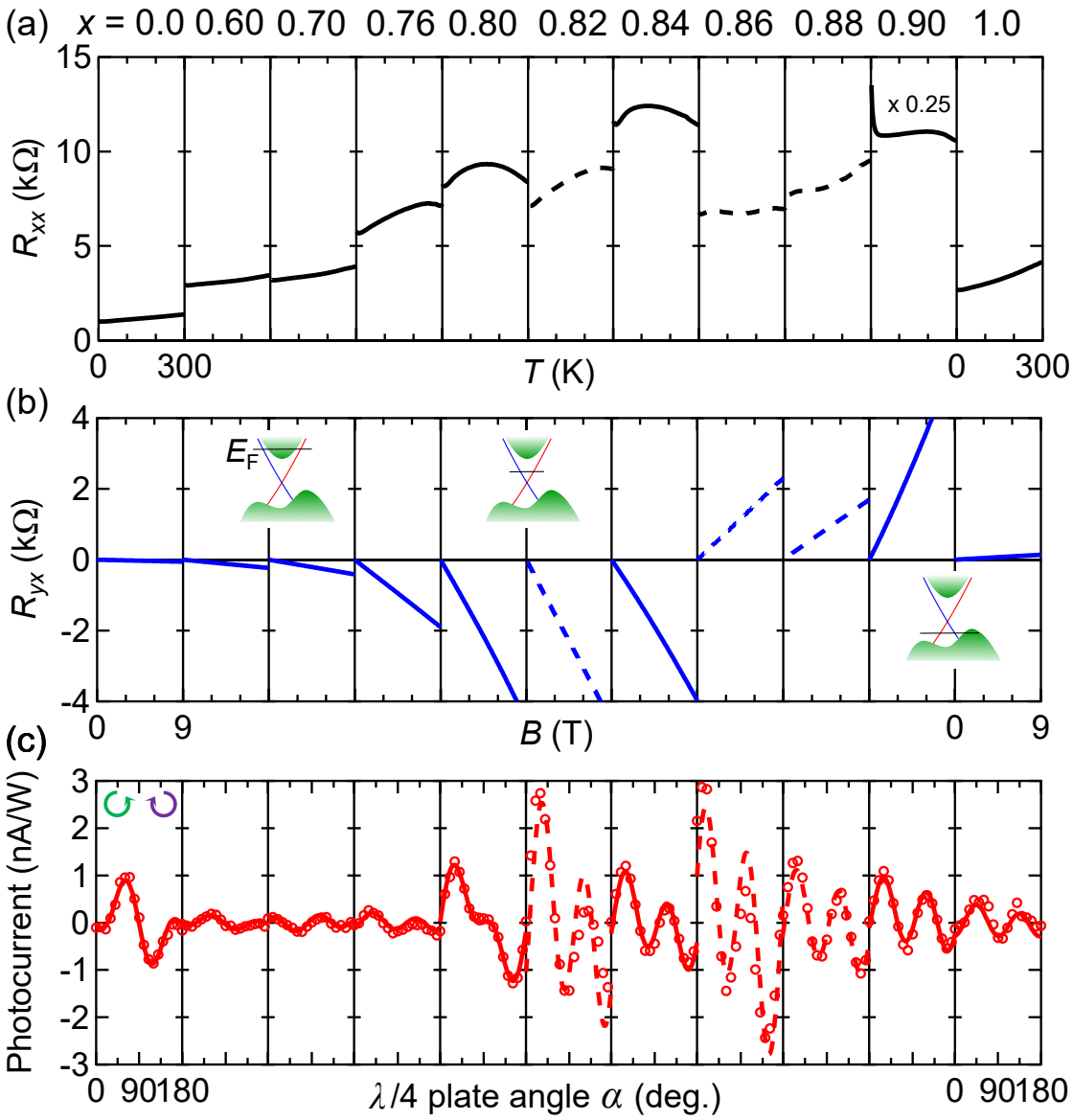

Figure 3.6: Evolution of the transport properties and CPG effect by tuning E_F in BST thin films. (a) Temperature dependence of the longitudinal resistance R_{xx}. (b) Field dependence of the Hall resistance R_{yx} at $T = 2$ K. (c) Polarization-dependent photocurrent measured at $\theta = 45$ deg. and $\varphi = 0$ deg. The solid lines represent fitting by Eq. (3.3) in the text. The data represented with dashed lines correspond to the samples fabricated in a different chamber condition.

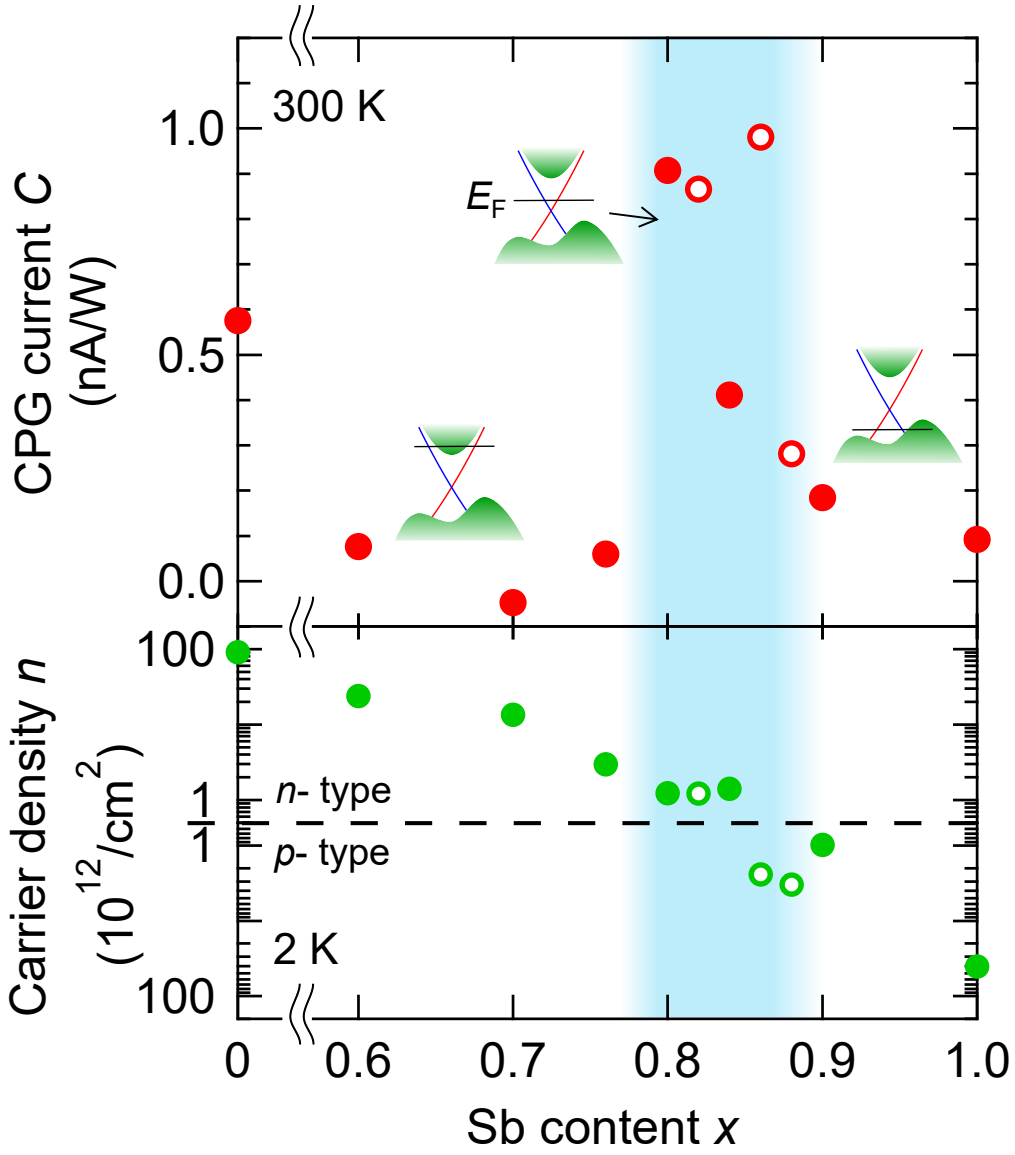

Figure 3.7: CPG current and carrier density as a function of Sb content x. The carrier density is estimated at $T = 2$ K to avoid contributions from thermally-activated carrier. The samples represented by open circles were fabricated in a different chamber condition. The colored area indicates that E_F locates in the band gap.

To see the impact of E_F on the CPG effect, we present the light-polarization dependence of the photocurrent for all the samples in the bottom panel of Fig. 3.6 (Fig. 3.6(c)). Note that the polarization-independent component, corresponding to D in Eq. (3.3), is subtracted here. In Fig. 3.7 we show the variation of the CPG

current (C in Eq. (3.3)) with the Sb content x, in comparison with the carrier density estimated by $n = 1/e|R_{\mathrm{H}}|$. Figures 3.6(c) and 3.7 obviously indicate that CPG current is larger when E_{F} locates within the band gap ($x = 0.80$–0.88, see the colored area in Fig. 3.7) than in the bulk conduction or valence bands ($x = 0.60$–$0.76, 0.90$, and 1.0) except the n-type end compound ($x = 0.0$), although the magnitude of the signal seems to depend on the position of E_{F} in the band gap.

3.3.2 Discussions

First, we discuss the origin of the enhanced CPG effect while E_{F} lies within the band gap. If we neglected the scattering effect, the CPG current would be the sum of the contributions from all the excited electrons and holes generated by optical transitions. However, we should note that in the presence of scattering photo-excited carrier away from the Fermi level quickly relaxes, leading to small contributions to the current. Therefore, it would be a reasonable scenario that the CPG current is mainly carried by electrons and holes excited near the Fermi level (Fig. 3.8(b)). From that viewpoint, we attribute the enhanced CPG effect to suppressed scattering of surface Dirac electrons to the bulk channel (Figs. 3.8). When E_{F} lies in the bulk band, photo-excited surface carrier at the Fermi level are easily absorbed into bulk states through phonon or impurity scattering [62–65] (Fig. 3.8(a)), resulting in the small or negligible CPG currents ($x = 0.60$–$0.76, 0.90$ and 1.0) (Fig. 3.7). On the other hand, once E_{F} is tuned within the bulk band gap ($x = 0.80$–0.88), surface carrier at the Fermi level are not scattered to bulk states but only to surface states, where perfect back-scattering is prohibited due to the spin-momentum locking (Fig. 3.8(b)). That is why the CPG current notably evolves in the in-gap region (see the colored area in Fig. 3.7). We also stress that the enhancement is irrelevant with the amount of light absorption; we confirmed that absorption coefficient is almost unchanged for the relevant compounds ($x = 0.60$–1.0) (Fig. 3.9).

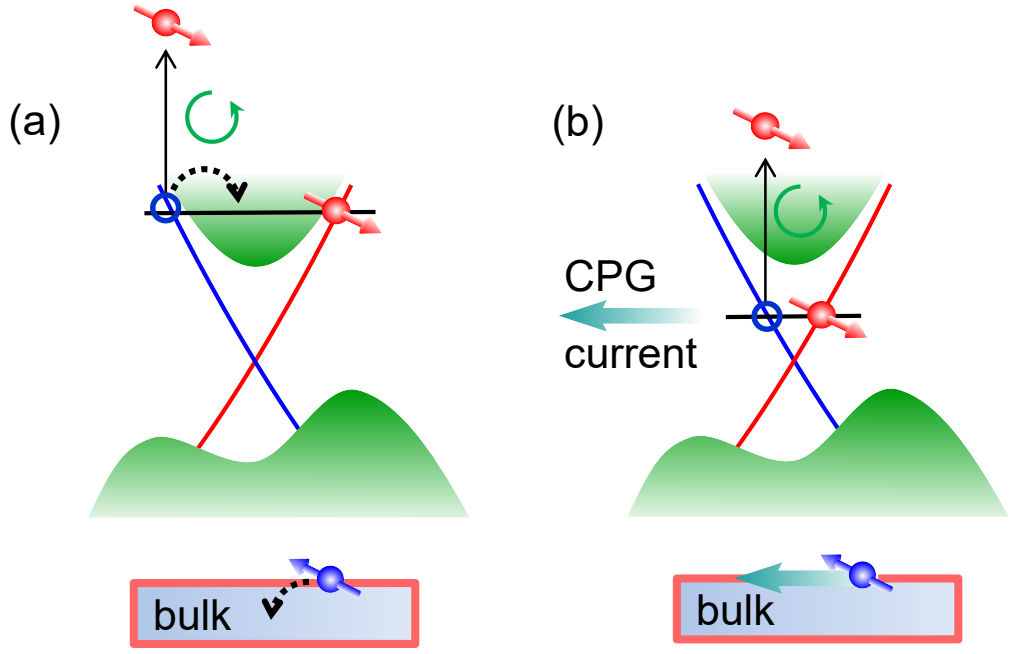

Figure 3.8: Schematic illustrations of the CPG effect when E_F locates (a) in the bulk conduction band and (b) within the band gap.

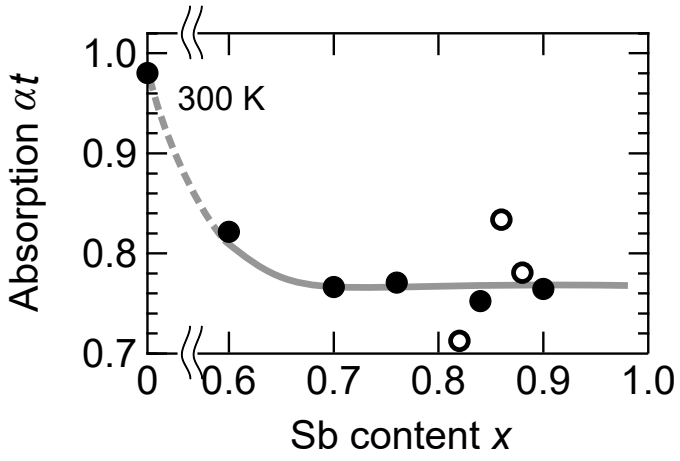

Figure 3.9: Composition dependence of absorption coefficient in BST films for $\hbar\omega = 1.17$ eV, the same photon energy that we employed in the photocurrent experiment. The measurement was conducted at room temperature. As in Fig. 3.7, the open circles correspond to the samples fabricated in a different chamber condition. The line is a guide to the eyes.

Then, we focus on the behavior within the in-gap region (see the colored area in Fig. 3.7). Figure 3.7 suggests that for E_{F} inside the band gap, the CPG current seems to change depending on the position of E_{F}, although still apparently larger than the signals for E_{F} outside the band gap. However, we speculate that this is not an intrinsic effect of E_{F}, but rather reflect the sample dependence of disorder strength that unintentionally occurred during the growth process. Indeed, for the in-gap region, the CPG current seems to be roughly scaled to scattering time of the surface states (Fig. 3.10). Here the scattering time τ is deduced from the carrier density and conductance of the surface Dirac electrons estimated by the resistance measurements (Figs. 3.6(a) and 3.6(b)), through a conventional formula by the Boltzman equation, $\sigma_{xx}^{\mathrm{surface}} = \frac{1}{2}e^2\tau v^2 D(E_{\mathrm{F}})$. Here $\sigma_{xx}^{\mathrm{surface}}$ represents the conductance of the surface Dirac electrons, v the group velocity, $D(E_{\mathrm{F}})$ the density of states at E_{F}. Note that in the case of two-dimensional Dirac electrons, $D(E_{\mathrm{F}})$ is written down with the carrier density n as $D(E_{\mathrm{F}}) = \frac{1}{\hbar v_{\mathrm{F}}}\sqrt{\frac{n}{\pi}}$.

Under the aforementioned assumption that photocurrent is carrried by the excited carrier near E_{F}, we expect the CPG current to be approximately proportional to the conductance of the surface states, $\sigma_{xx}^{\mathrm{surface}}$. Therefore, in an ideal case without any variation of disorder strength, we think that as E_{F} gets closer to the DP, $\sigma_{xx}^{\mathrm{surface}}$ and hence the CPG current would decrease as scaled to $D(E_{\mathrm{F}})$. To investigate such an intrinsic variation of the CPG current for the in-gap region, fine field-effect control of E_{F} on a single sample would be necessary as well as low-temperature measurement.

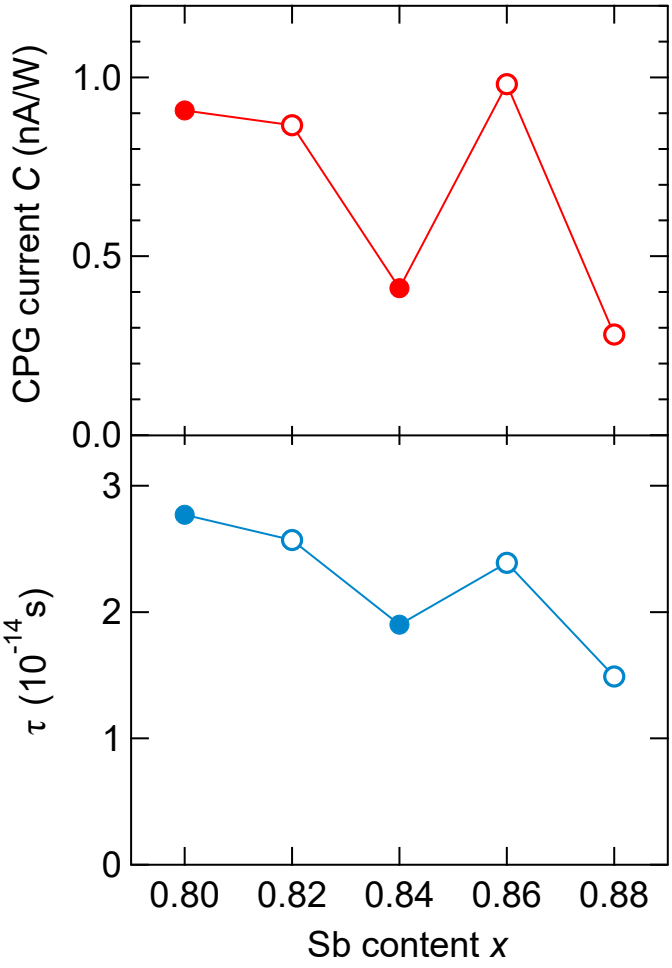

Figure 3.10: CPG current and scattering time of surface Dirac electrons for BST films with E_F located within the band gap. As in Fig. 3.7, the open circles correspond to the samples fabricated in a different chamber condition.

For $x = 0.0$ (Bi_2Te_3), sizable CPG current appears despite the Fermi level deep into the bulk conduction band (Fig. 3.7). This might be related to another non-trivial surface band with spin–momentum locking that locates about 1-eV higher than E_F in Bi_2Te_3 [66]. We speculate that unlike other compounds with the lower E_F ($x = 0.60$–0.76), circularly-polarized light excites bulk and surface electrons at the Fermi level up to the vacant surface band, resulting in an asymmetric carrier distribution in the momentum space. As a result, a significant amount of bulk hole carrier generated at E_F would contribute to the CPG current, leading to the large signal (Fig. 3.7).

We also note that the sign of the CPG current remains unchanged while E_F

traverses across the DP (Fig. 3.7), although the spin helicity changes. Here we note that the CPG current for $x = 0.70$ shows a small negative value (Fig. 3.7), but it is difficult to quantitatively discuss this point because its amplitude is close to our experimental resolution. The constant sign of the CPG current is quite reasonable because (i) the direction of the photocurrent is determined by the group velocity of excited carrier at E_{F}, and (ii) the group velocity for electrons with a specific spin orientation has the same sign, irrespective of their energies relative to the DP. Therefore, photo-carriers with the specific spin state generated by circularly-polarized photons should flow in the same direction. This has also been reported in other spin–charge conversion experiments [32, 67].

The maximal yield of the CPG current observed by fine E_{F}-tuning in this work is around 10 $\mathrm{pAW^{-1}cm^2}$, divided by energy flux per unit area of the incident laser. This is several times larger than the reported value in Bi_2Se_3 thin flakes [43]. Furthermore, by normalizing the CPG current by the number of photons absorbed, we find out that the generation efficiency is twenty times as large as that for Bi_2Se_3 flakes [43], despite some differences in experimental conditions.

As compared with semiconductor quantum wells, the maximal generation efficiency in our study is comparable to the typical reported values (1–100 $\mathrm{pAW^{-1}cm^2}$) [54, 68, 69]. However, we should take into account much stronger disorder in our sample; the mobility of the surface Dirac electrons in our E_{F}-tuned BST films is orders-of-magnitude lower than those of quantum wells. In this aspect we can regard that the efficiency obtained in our experiment is remarkably large, which might be ascribed to the absence of the cancellation between the two Fermi surfaces as mentioned in Secs. 1.2 and 3.1.2. We expect that further improvement in TI growth would potentially yield the CPG current far beyond the typical values in semiconductor quantum wells.

3.4 Back illumination results

Finally, we discuss the potential contribution from the bottom surface states, which reside at the interface between the film and the substrate. Since the film thickness (8 nm) is comparable to the penetration length of the laser, some amount of CPG current at the bottom surface may contribute to the observed signal. Here we should note that the Dirac cone of the bottom surface has the opposite spin helicity and hence show the oppositely-directed CPG current to that of the top surface (see also Fig. 3.11(a)).

To clarify the contribution from the bottom surface, we measured CPG current for the bottom surface illumination. Figure 3.11(c) presents the incident angle dependence of the CPG current for front (Fig. 3.11(a)) and back surface illumination (Fig. 3.11(b)) on BST films of $x = 0.84$, 0.86 and 0.88. For the back illumination, we define the incident angle ψ, whose positive direction is opposite to that of θ (Figs. 3.11(a) and 3.11(b)). As indicated by Eq. (3.2), incident angle dependence of the CPG current is determined by $e_{||}I$, where $e_{||}$ and I are the in-plane projection of the unit vector $\mathbf{e}$ representing the light propagation direction and the intensity of the light, respectively. Indeed, we confirmed that this term nicely fits the observed angle dependence (see the solid lines in Fig. 3.11(c)).

If both surface states generated CPG current with equal efficiency, the sign of the CPG current for the back illumination ($\psi > 0$) would be opposite to that for the front illumination ($\theta > 0$). However, it turned out to be the same for all three samples (Fig. 3.11(c)). As a result, we find that for both geometries CPG current from the top surface dominates that from the bottom surface. This means that the bottom surface is less capable of generating CPG current than the top surface. We speculate that such inequivalence between the top and bottom surface would be ascribed to strong disorder on the substrate surface.

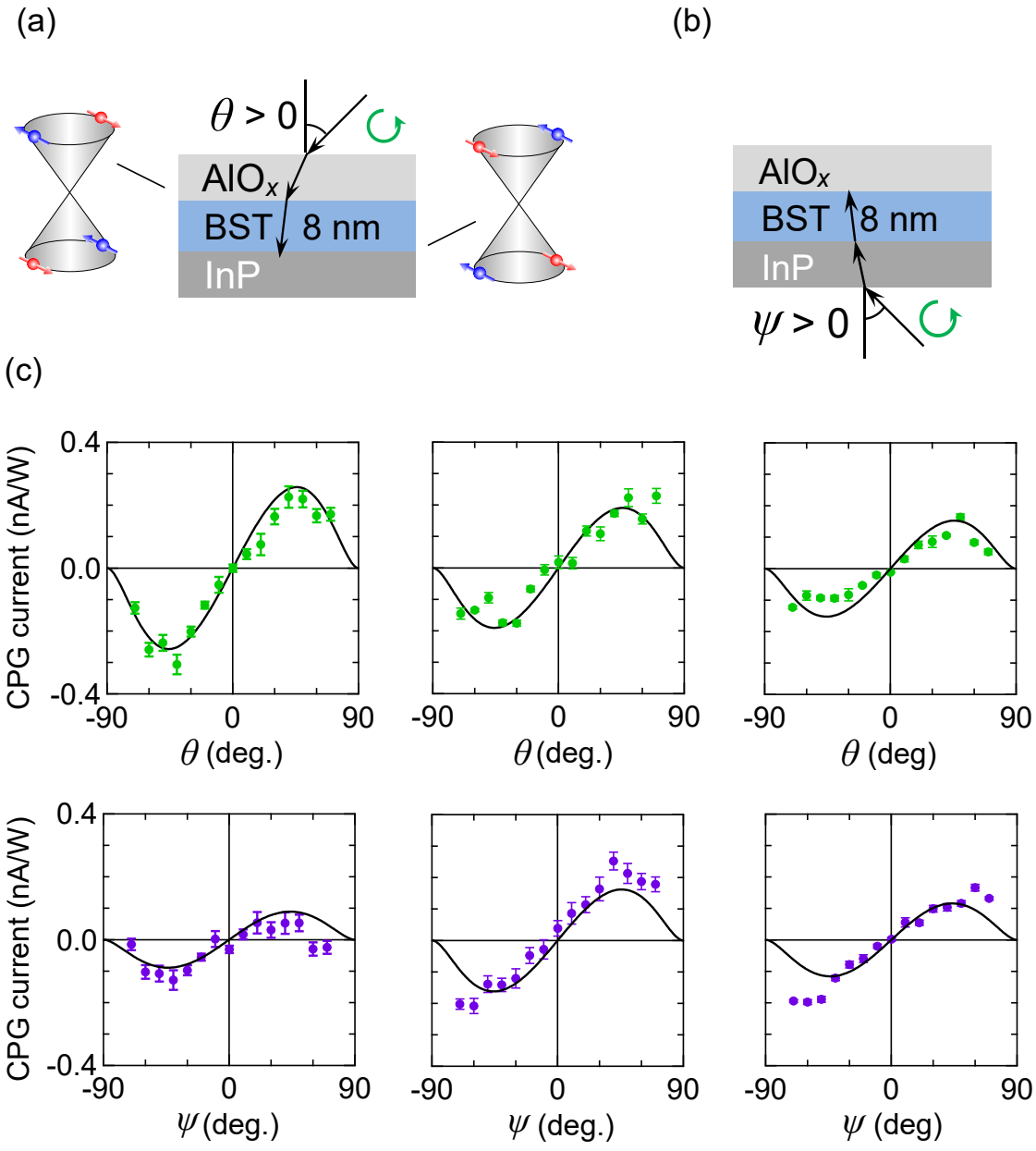

Figure 3.11: (a), (b) Schematic illustrations of (a) front and (b) back illumination experiments. (c) Incident angle dependence of the CPG current in BST films of x = 0.84 (left), 0.86 (middle) and 0.88 (right) for front (top panel) and back (bottom panel) illuminations. The solid lines represent the theoretical fit (see the text).

3.5 Summary

In this Chapter we uncover the characteristic E_{F}-dependence of the CPG effect on TI thin films and achieve the remarkable enhancement for E_{F} located within the band gap. We attribute the enlarged CPG effect to suppressed scattering of the surface Dirac electrons to the bulk states. We also find out that the generation efficiency amounts to the same order of magnitude as the typical values in semiconductor quantum wells, despite the much-lower mobility.

Chapter 4

Quantized magneto-optical effect on quantum anomalous Hall states

4.1 Introduction

In this Chapter we present the quantization of magneto-optical Faraday and Kerr rotations on quantum anomalous Hall (QAH) states in topological insulator (TI) thin films, where those rotation angles are related with each other through a universal equation determined by the fine-structure constant α.

4.1.1 Quantized magneto-optical rotations on quantum anomalous Hall states

As stated in Sec. 1.3 surface Dirac electron states coupled with magnetization normal to the TI surface exhibit QAH effect, i.e., $\sigma_{xy} = e^2/h$ and $\sigma_{xx} = 0$ at zero magnetic field, due to the divergent Berry curvature at the Dirac point. On the other hand, the Kubo formula for optical conductance suggests that the quantization of d.c. Hall conductance persists for finite frequency, as long as the energy is well below the mass gap at the Dirac point:

$$\sigma_{xy}(\omega) = e^2/h,\ \sigma_{xx}(\omega) = 0. \tag{4.1}$$

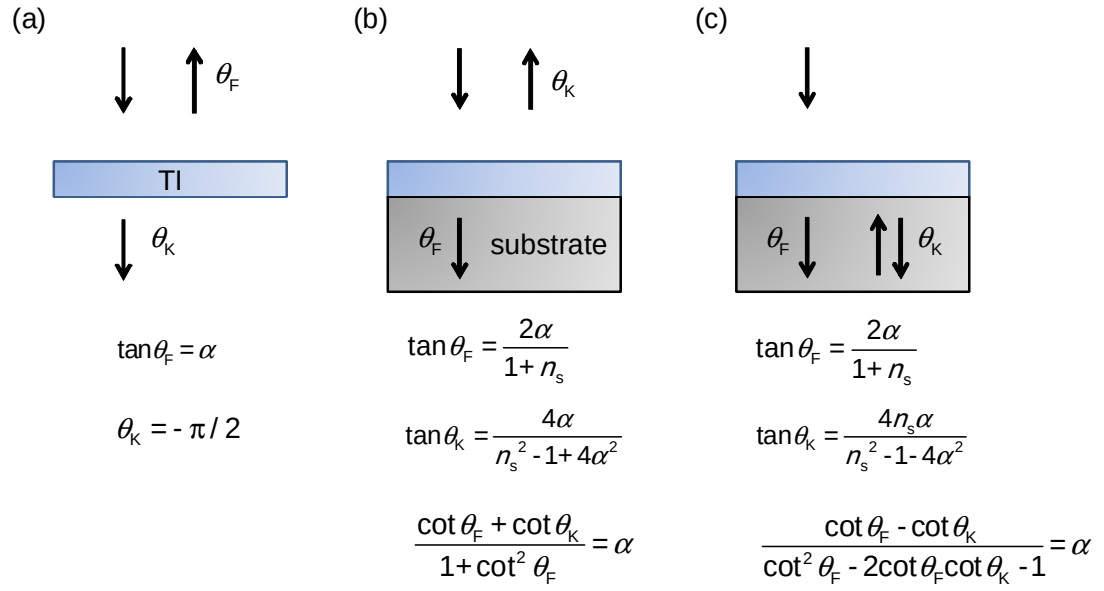

Figure 4.1: Schematic illustrations of various experimental geometries for quantized magneto-optical effect and the corresponding Faraday ($\theta_{\rm F}$) and Kerr ($\theta_{\rm K}$) rotation angles, together with their universal relationships. (a) corresponds to free-standing TI. (b) and (c) corresponds to TI thin film on substrate (b) in a common magneto-optical experiment and (c) time-domain spectroscopy as we employ in this Chapter. α and $n_{\rm s}$ denote the fine-structure constant and refractive index of substrate, respectively.

In general, transverse optical responses in the presence of magnetic field or magnetization along the light propagation direction produce rotation of photon polarizations in transmitted and reflected light, corresponding to magneto-optical Faraday and Kerr rotations. In the case of the QAH effect with the quantization of Hall conductance (Eq. (4.1)) simple algebra shows that for photon wavelength much larger than the TI thickness, Faraday and Kerr rotation angles take the following universal values with the fine-structure constant α (Fig. 4.1(a)) [41, 70]:

$$\theta_{\rm F} = \alpha \tag{4.2}$$

$$\theta_{\rm K} = -\pi/2, \tag{4.3}$$

although the angles are modified in the case of TI on substrates (Figs. 4.1(b) and 4.1(c)) (see Sec. 4.1.2).

We stress that those quantizations of magneto-optical Faraday and Kerr rotations can be regarded as a quantum phenomenon, along with the Hall conductance quantization in quantum (anomalous) Hall insulators and flux quantization in superconductors.

4.1.2 Substrate effect on quantized magneto-optical rotations

The quantized rotation angles presented in Eqs. (4.2) and (4.3) correspond to the case of a free-standing TI exhibiting QAH effect (Fig. 4.1(a)). For a TI thin film on a substrate, which is much more feasible and realistic than the free-standing one, those quantized rotation angles are modified by the refractive index of the substrate $n_{\rm s}$, while they are still correlated with each other by a universal relationship defined by the fine-structure constant α (Figs. 4.1(b) and 4.1(c)).

For a common geometry of magneto-optical experiment schematically shown in Fig. 4.1(b) [71], the Faraday and Kerr rotation angles are expressed as

$$\theta_{\rm F} = \frac{2\alpha}{1+n_{\rm s}} \tag{4.4}$$

$$\theta_{\rm K} = \frac{4\alpha}{n_{\rm s}^2-1+4\alpha^2}. \tag{4.5}$$

As a consequence, a universal relationship between the two is deduced as

$$\frac{\cot\theta_{\rm F}+\cot\theta_{\rm K}}{1+\cot^2\theta_{\rm F}} = \alpha. \tag{4.6}$$

On the other hand, for the time-domain spectroscopy (TDS) as we employ in this Chapter, Kerr rotation is measured for light that is reflected at the back-surface of the substrate after transmission of the thin film (see Fig. 4.1(c)). As a result, in the geometry of TDS the Kerr rotation angle is described as

$$\theta_{\rm K} = \frac{4n_{\rm s}\alpha}{n_{\rm s}^2-1-4\alpha^2}, \tag{4.7}$$

while the Faraday rotation angle is expressed by Eq. (4.4) as well. Hence, the universal relationship is replaced by the following equation:

$$\frac{\cot\theta_{\rm F}-\cot\theta_{\rm K}}{\cot^2\theta_{\rm F}-2\cot\theta_{\rm F}\cot\theta_{\rm K}-1} = \alpha. \tag{4.8}$$

To observe the quantized magneto-optical effect on the QAH states, probing with photon energy well below the mass gap in the Dirac surface states is necessary. The size of the mass gap has been reported to range from 22 meV for a Cr-doped Sb_2Te_3 thin film [72] to 50 meV for a $Cr_y(Bi_{1-x}Sb_x)_{2-y}Te_3$ (CBST) bulk single crystal [73]. Therefore, magneto-optics by the terahertz (THz) spectroscopy probing the lower-energy range, e.g., 1–8 meV in the present experiment, would be suitable. Furthermore, magnetic modulation-doping in CBST thin film has been lately found to dramatically widen the observable temperature region of QAH effect up to several Kelvin, making it feasible to approach the QAH state [26]. Thus, in this Chapter, to observe the quantized Faraday and Kerr rotation angles on QAH states, we perform THz magneto-optics on CBST thin films with the magnetic modulation-doping.

4.2 Observation of quantum anomalous Hall effect

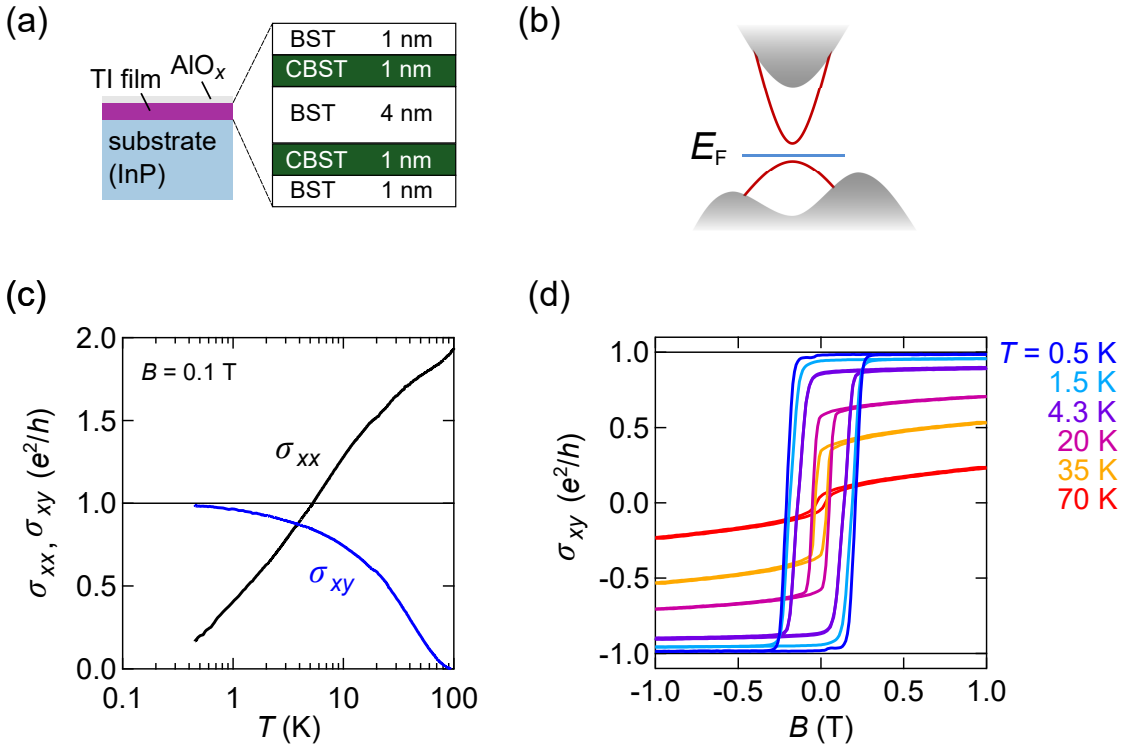

Figure 4.2: (a), (b) Schematics of CBST thin film with magnetic modulation doping (a) and of the massive Dirac surface states under the presence of the perpendicular magnetization (b). (c) Temperature dependence of the longitudinal (σ_{xx}) and Hall (σ_{xy}) conductances at $B = 0.1$ T. (d) Magnetic field dependence of σ_{xy} at various temperatures.

Figure 4.2(a) shows a schematic illustration of the CBST thin film with the magnetic modulation-doping. In this TI film a rich amount of Cr are doped in each quintuple-layer(QL) just below/above the topmost/bottommost QL. Evolution of the magnetization induced by Cr-doping gives rise to the QAH state (Figs. 4.2(c) and 4.2(d)). The ferromagnetic transition occurs around $T_C \sim 70$ K with the onset of the anomalous Hall term in σ_{xy} (Fig. 4.2(c)). As temperature decreases, σ_{xy} develops and tends to saturate at the quantized value e^2/h at $T \sim 0.5$ K, while σ_{xx} steeply decreases towards zero (Fig. 4.2(c)). The Hall angle (σ_{xy}/σ_{xx})

becomes as large as 1 around 4 K, turning into the QAH regime at temperatures more than an order of magnitude higher [26] than uniformly Cr- or V- doped TI films [21–25]. This is due perhaps to enlargement of the mass gap induced by the rich Cr-doping and the reduced disorder by Cr in the topmost and bottommost layers. As shown in Fig. 4.2(d), hysteric behaviors of Hall conductance against magnetic field also evidences the development of the QAH regime. The fully-quantized σ_{xy} at the lowest temperature indicates that the Fermi energy locates well within the magnetic mass gap of the surface Dirac dispersion (Fig. 4.2(b)), without an additional field-effect tuning.

4.3 Quantized Faraday and Kerr rotations on quantum anomalous Hall states

4.3.1 Magneto-optical polarization rotations in terahertz waveform

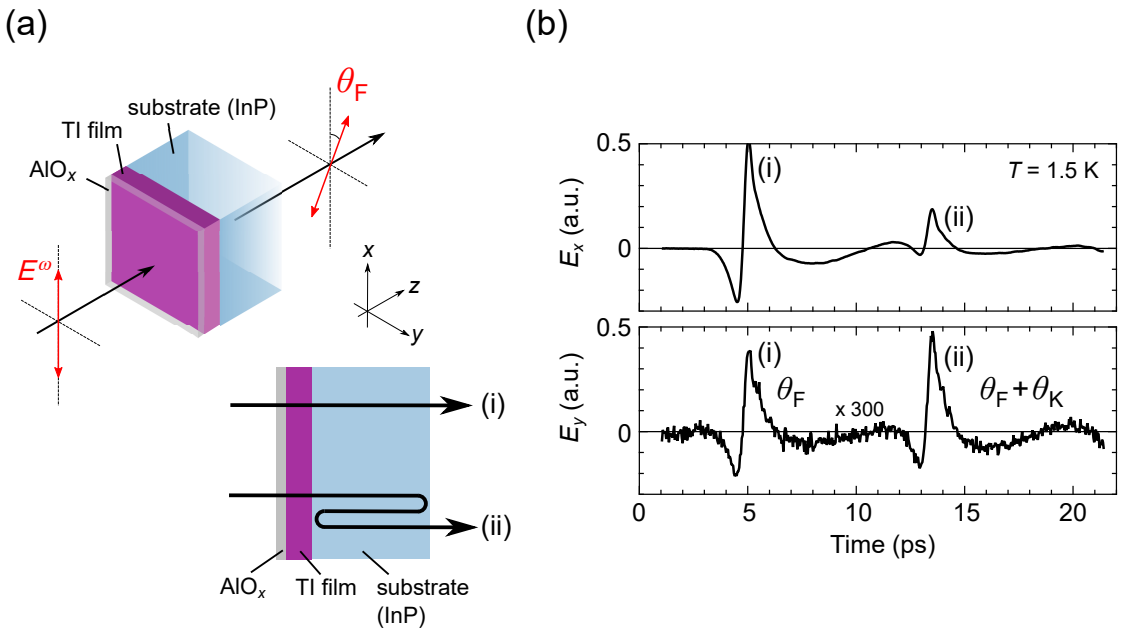

Figure 4.3: (a) Schematics of the THz magneto-optics for the CBST thin film. Faraday and Kerr rotations are measured by the first THz pulse (i) and the second THz pulse (ii), respectively. (b) Time evolution of THz pulses going through the magnetic TI film at $B = 0$ T (see Sec. 2.4 for details). E_x and E_y are transmitted light with polarization parallel and perpendicular to that of the incident light, respectively. The first pulse (i) is the light directly transmitted through the TI film and substrate, while the second pulse (ii) corresponds to the light once reflected at the back-surface of substrate. The second pulse (ii) experiences the Kerr rotation θ_K at the back-surface of the TI film in addition to the Faraday rotation θ_F.

THz-TDS allows magneto-optical measurements with sufficiently lower photon energy (1–8 meV) than the mass gap of the surface Dirac states (20–50 meV [72, 73]) and with high resolution of light polarization rotations (< 1 mrad). The measurement configuration of magneto-optics by THz-TDS is schematically

illustrated in Fig. 4.3(a) (see Sec. 2.4 for details). Depending on the time delay, the monocycle THz pulse can differentiate the directly transmitted pulse (i) and the delayed pulse generated by reflection at the back-surface of the substrate (ii) (see Figs. 4.3(a) and 4.3(b)); this enables us to separably measure Faraday and Kerr rotations, as reported for TI thin films [46,48] and graphene on substrate [74].

As shown in Fig. 4.3(b), the temporal waveform of $E_y(t)$ shows pronounced rotation of polarization on the first pulse (i) as well as on the second one (ii) due to the presence of the magneto-optical rotations at zero external magnetic field. The first pulse (i) involves the Faraday rotation (θ_{F}), while the second pulse (ii) is composed of θ_{F} plus the Kerr rotation (θ_{K}) experienced at the back-surface of the magnetic TI film (Fig. 4.3(b)).

4.3.2 Transmittance spectra

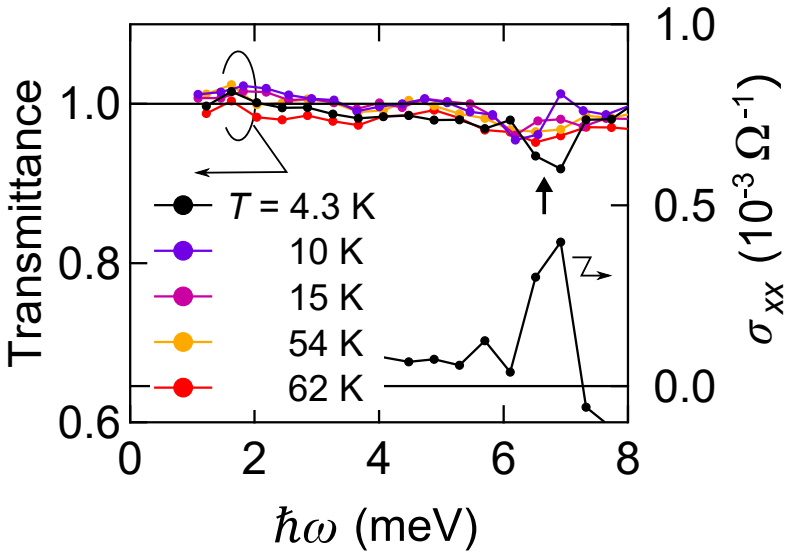

Figure 4.4: Transmittance (left ordinate) spectra of the magnetic TI film at various temperatures and optical conductance (right ordinate) σ_{xx} spectrum at $T = 4.3$ K.

The transmittance spectra obtained by $E_x(t)$ at different temperatures are shown in Fig. 4.4. The transmittance is close to unity without any discernible absorption, except for dips around 7 meV indicated by an arrow; see also the peak in

optical conductance σ_{xx} at $T = 4.3$ K plotted together in Fig. 4.4. From comparison with a previous optical study on BST films [75], we assign this transmittance dip to the optical phonon mode of BST. For derivation of the transmittance and optical conductance, see Sec. 2.4. The negligibly-weak absorption is consistent with the fact that the Fermi energy locates within the mass gap of the surface Dirac cone, indicated by the QAH effect observed at d.c. limit (Fig. 4.2(b)).

4.3.3 Magneto-optical Faraday and Kerr rotation spectra

Fourier transformation of the electric field pulses $E_x(t)$ and $E_y(t)$ (Fig. 4.3(b)) provides the Faraday and Kerr rotation spectra, $\theta_{\rm F}(\omega)$ and $\theta_{\rm K}(\omega)$, as well as the corresponding ellipticity spectra, $\eta_{\rm F}(\omega)$ and $\eta_{\rm K}(\omega)$ (Figs. 4.5(a) and 4.5(b)). See Sec. 2.4 for the details of the derivation. At $T = 1.5$ K the rotation angle spectra, $\theta_{\rm F}(\omega)$ and $\theta_{\rm K}(\omega)$ show finite values around 2 and 6 mrad, respectively, with a modest frequency dependence (Figs. 4.5(a) and 4.5(b)). The corresponding ellipticity spectra, $\eta_{\rm F}(\omega)$ and $\eta_{\rm K}(\omega)$, are close to zero in the whole photon-energy range (< 8 meV). Note that noise-like fringe structures in the Kerr rotation spectra (Fig. 4.5(b) and Fig. 4.6(a)), unlike the almost ω-constant Faraday rotation spectra, should come from inevitable interference effect due to the temporal overlap with the early-coming Faraday rotation signals (see Fig. 4.3(b)). Those characters, i.e., little frequency dependence and near-zero ellipticity, strongly indicate that the current THz energy window (1–8 meV) is well below the threshold energy for any magneto-optically active real transitions. This is consistent with the fact that the magnetic mass gap on the Dirac point (reported to be 20–50 meV by STM [72, 73]) is sufficiently large as compared to the energy range of this measurement. Note also that cyclotron resonance, which has been observed in previous magneto-optical studies on TIs [46–52], is absent in the present measurement because of zero external magnetic field.

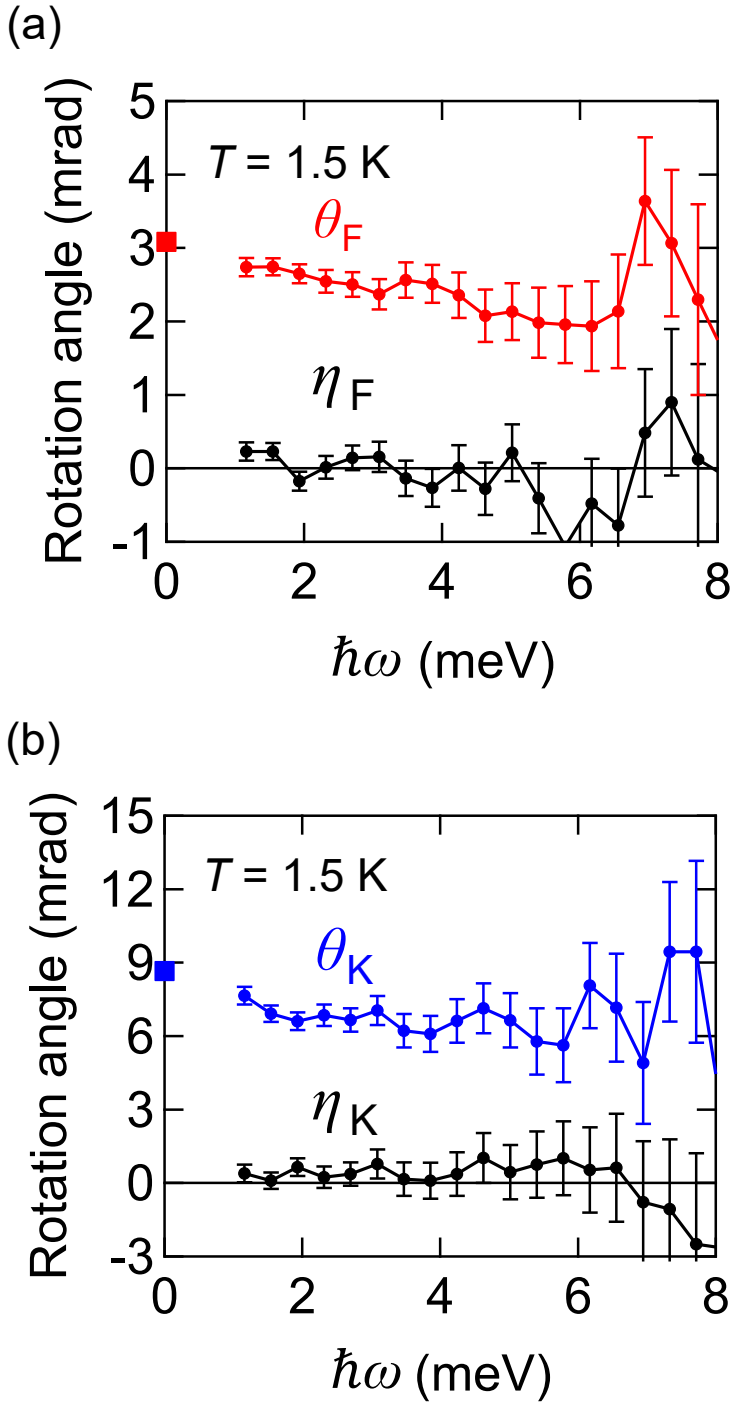

Figure 4.5: The rotation angle $(\theta_{\rm F}, \theta_{\rm K})$ and ellipticity spectra $(\eta_{\rm F}, \eta_{\rm K})$ for the magneto-optical (a) Faraday and (b) Kerr rotations at $T = 1.5$ K (see Sec. 2.4 for the derivation). The error bars are evaluated by standard error of the mean (s.e.m.) of several runs of measurement. The rotation angles at $\omega = 0$ calculated from the d.c. transport data (Fig. 4.2(d)) are also plotted on the left ordinates.

Furthermore, the observed Faraday and Kerr rotation angles are quantitatively consistent with the rotation angles at d.c. limit (Figs. 4.5(a) and 4.5(b)) that are calculated from σ_{xx} and σ_{xy} obtained by the d.c. transport measurement (Fig. 4.2(d)) through the following formulas [50, 74]:

$$\theta_{\mathrm{F}} = \frac{1}{2}\arg\left[\frac{t_-}{t_+}\right] \quad \left(t_\pm = \frac{2}{1+n_{\mathrm{s}}+Y_\pm}\right) \tag{4.9}$$

$$\theta_{\mathrm{K}} = \frac{1}{2}\arg\left[\frac{r_-}{r_+}\right] \quad \left(r_\pm = \frac{-1+n_{\mathrm{s}}-Y_\pm}{1+n_{\mathrm{s}}+Y_\pm}\right). \tag{4.10}$$

Here, $t_\pm(\omega)$ and $r_\pm(\omega)$ represent the transmittance and reflection coefficients of right- and left-handed circularly-polarized light, respectively. The admittance $Y_\pm$ are described as $Y_\pm = Z_0(\sigma_{xx} \pm i\sigma_{xy})$ and n_{s} is the refractive index of the InP substrate. We determined n_{s} as 3.47 by measuring THz response of the substrate, which well agrees with literature [76]. For instance, the estimated rotation angles for $\theta_{\mathrm{F}}(\omega)$ and $\theta_{\mathrm{K}}(\omega)$ at $\omega = 0$ are around 3 and 9 mrad at 1.5 K (indicated with closed squares on the respective ordinates in Figs. 4.5(a) and (b)). This quantitative agreement with the d.c. Hall conductance exemplifies that the observed THz rotation stems from the QAH effect on the TI surfaces.

Since the magnetic-layer thickness in the present film is 2 nm in total, the figure of merit for the observed Faraday rotation can be effectively estimated as $\sim 7 \times 10^5$ degree/cm. In comparison, the Faraday rotation angle in a typical Faraday rotator, Bi-doped yttrium iron garnet (YIG) is about 9×10^2 degree/cm around 1 eV [77]. This indicates that the rotation angle observed here is remarkably large as compared to those for conventional ferromagnets in the off-resonant condition. Furthermore, we confirmed nearly the same magnitude of rotation angles on another magnetic TI film with twice the thickness of magnetic layer (4 nm in total) (see Appendix). These results strongly indicate that the polarization rotations observed here intrinsically originate from the response of the TI surface states rather than bulk responses.

4.3.4 Temperature evolution of Faraday and Kerr rotation spectra

Figure 4.6(a) shows the temperature evolution of the Faraday and Kerr rotation spectra. The rotation angles decrease with increasing temperature and vanish at T_C (see also Fig. 4.6(b)), in accord with the disappearance of the ferromagnetic state.

In Fig. 4.6(b) rotation angles at different temperatures, which are obtained by averaging the rotation angle spectra below ~ 4 meV, are displayed (closed circles) as a function of temperature. In Fig. 4.6(c) the same data are presented as a function of d.c. Hall conductance, together with the theoretical lines calculated from Eqs. (4.9) and (4.10) at $\omega = 0$. Note that open circles in Figs. 4.6(b) and 4.6(c) correspond to the rotation angles measured at $B = 1$ T (see Appendix). We also plot the data for the different sample at $T = 1.5$ K and $B = 0$ T (1 T) denoted by closed (open) triangles (see Appendix). In Fig. 4.6(c) the observed THz Faraday and Kerr rotation angles show a good agreement with the estimated $\omega = 0$ value, although small deviations are still discerned.

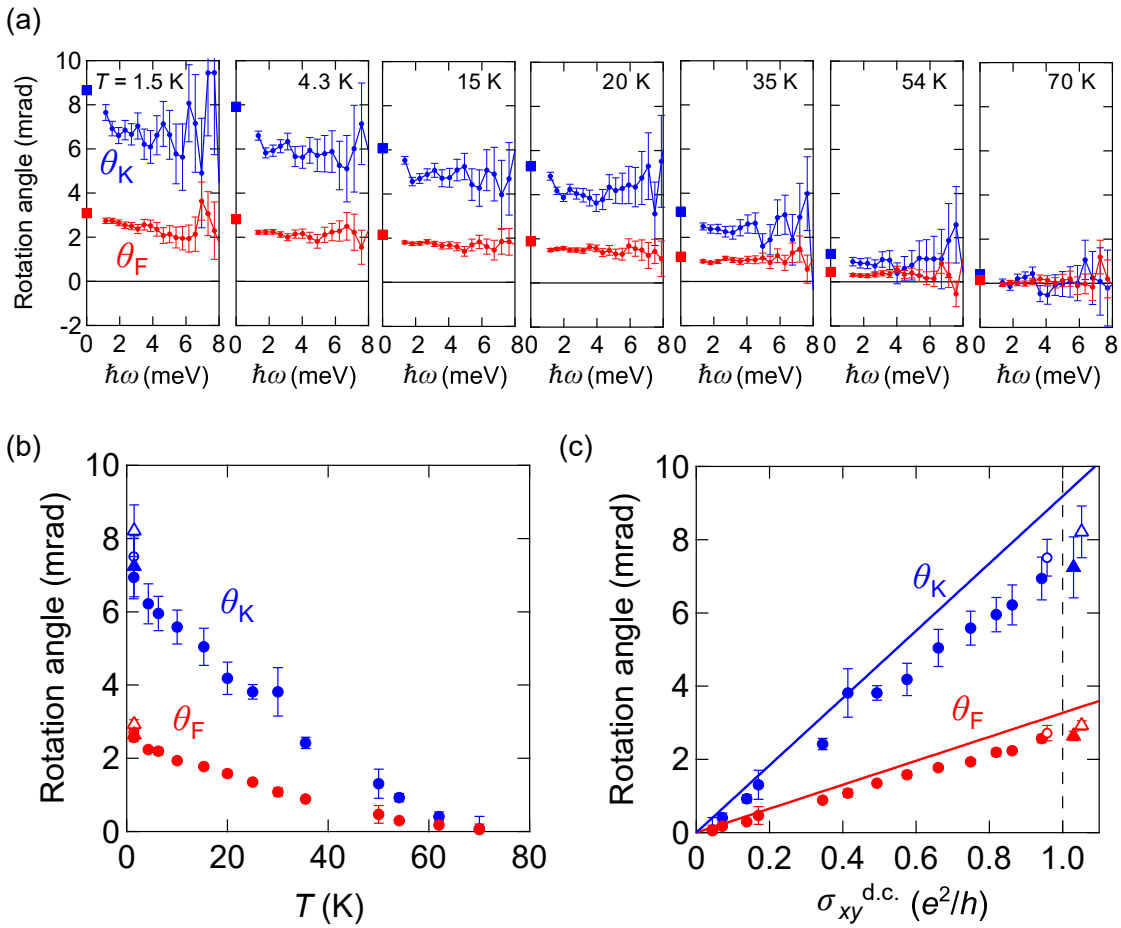

Figure 4.6: (a) Temperature dependence of the Faraday (red) and Kerr (blue) rotation spectra with the calculated $\omega = 0$ values on the ordinates. The error bars are evaluated by s.e.m. of several runs of measurement. (b), (c) The Faraday (red) and Kerr (blue) rotation angles as a function of (b) temperature and (c) d.c. Hall conductance. The rotation angles and the error bars are determined by the mean and standard derivative (s.d.) of the rotation angle spectra (a) below ~ 4 meV, respectively. The solid lines in (c) represent theoretical curves calculated from Eqs. (4.9) and (4.10) in the text.

4.4 Convergence to the fine-structure constant

As mentioned in Sec. 4.1, the relationship between the Faraday and Kerr rotation angles at the quantized limit has been predicted to lead to the fine-structure constant α, irrespective of any material parameters such as the dielectric constant and thickness of the film, capping layer and substrate. In our measurement geometry, the universal relationship between $\theta_{\rm F}$ and $\theta_{\rm K}$ in the QAH state coincides with Eq. (4.8). Here we define the left-hand side of Eq. (4.8) as a dimensionless function $f(\theta_{\rm F}, \theta_{\rm K})$:

$$f(\theta_{\rm F}, \theta_{\rm K}) = \frac{\cot\theta_{\rm F} - \cot\theta_{\rm K}}{\cot^2\theta_{\rm F} - 2\cot\theta_{\rm F}\cot\theta_{\rm K} - 1}. \tag{4.11}$$

In Fig. 4.7, we plot $f(\theta_{\rm F}, \theta_{\rm K})$ calculated from $\theta_{\rm F}$ and $\theta_{\rm K}$ (Fig. 4.6(c)) as a function of d.c. Hall conductance $\sigma_{xy}^{\rm d.c.}$. The black line denotes the theoretical curve estimated from Eqs. (4.9) and (4.10). As $\sigma_{xy}^{\rm d.c.}$ increases towards the quantized conductance with lowering temperature, $f(\theta_{\rm F}, \theta_{\rm K})$ approaches the universal value α, in good agreement with the theoretical line.

In Figs. 4.8, we show the trajectory of $\theta_{\rm F}$ and $\theta_{\rm K}$ towards the quantized values. It is overlaid on the color plot of the function $f(\theta_{\rm F}, \theta_{\rm K})$ in Fig. 4.8(a) and of the deviation of $f(\theta_{\rm F}, \theta_{\rm K})$ from α, $\frac{f(\theta_{\rm F},\theta_{\rm K})-\alpha}{\alpha}$ in Fig. 4.8(b). The dashed line and open star represent the ideal trajectory and quantized rotation angles expected from Eqs. (4.9) and (4.10), respectively. Those clearly indicate that $\theta_{\rm F}$ and $\theta_{\rm K}$ evolve along the ideal trajectory, with monotonic increase in $f(\theta_{\rm F}, \theta_{\rm K})$ towards α.

We should note that $\theta_{\rm F}$, $\theta_{\rm K}$ and $f(\theta_{\rm F}, \theta_{\rm K})$ are slightly smaller than the ideal values especially near the quantized limit (see Figs. 4.6(c), 4.7, 4.8(a) and 4.8(b)). In part, this is due to partial magnetization reversal during a measurement of a THz waveform under zero magnetic field, which takes a few tens of minutes. To avoid this effect, we performed the same measurements under magnetic field of $B = 1$ T at the lowest temperature. As a result, we obtained slightly higher values of Faraday and Kerr rotations and hence of $f(\theta_{\rm F}, \theta_{\rm K})$ (represented by open circles and triangles in Figs. 4.6(c), 4.7, 4.8(a) and 4.8(b)), although they still do not totally reach the quantized values.

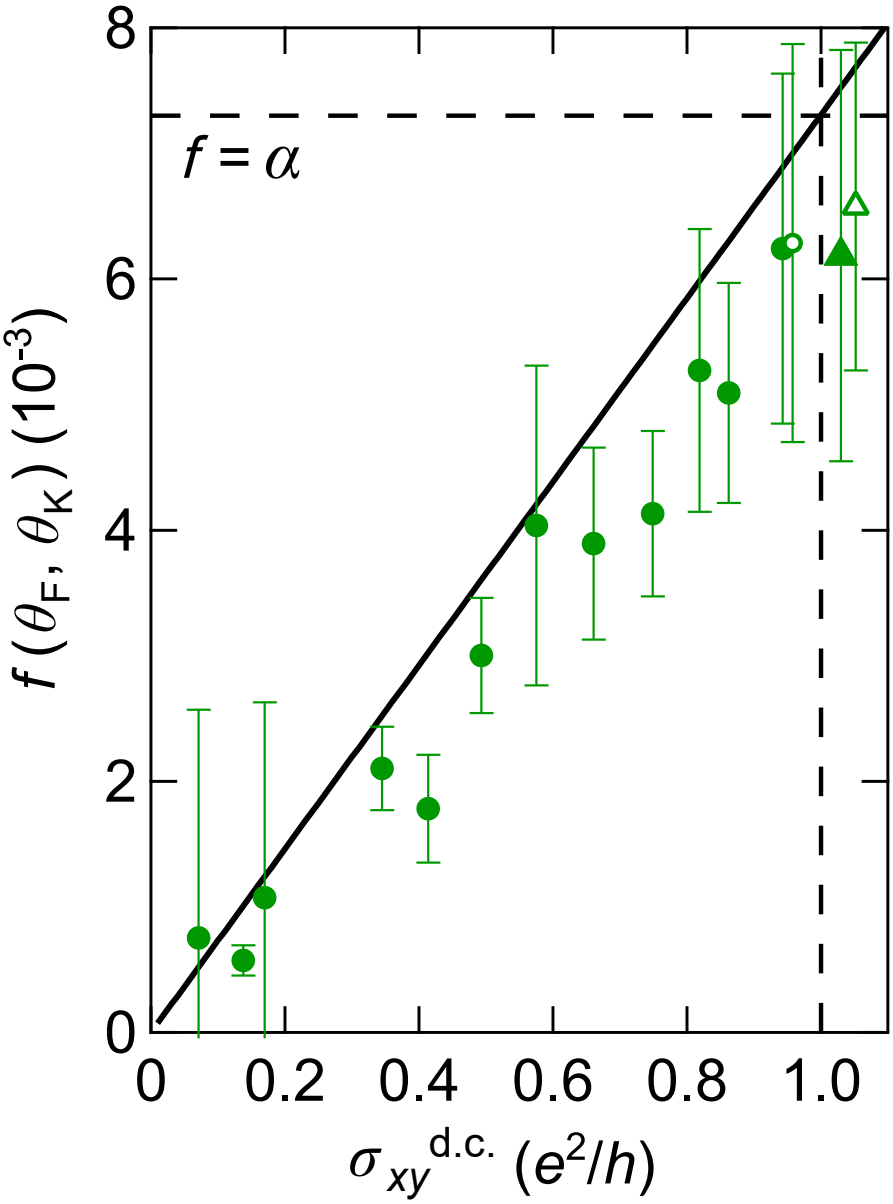

Figure 4.7: Evolution of the function $f(\theta_{\rm F}, \theta_{\rm K})$ (see Eq. (4.11) in the text) with increasing d.c. Hall conductance, $\sigma_{xy}^{\rm d.c.}$. The error bars are determined by the total derivative of $f(\theta_{\rm F}, \theta_{\rm K})$ calculated from the error bars of $\theta_{\rm F}$ and $\theta_{\rm K}$ presented in Figs. 4.6(b) and 4.6(c). α denotes the fine-structure constant. The solid line represents the theoretical curve deduced through Eqs. (4.9) and (4.10) in the text.

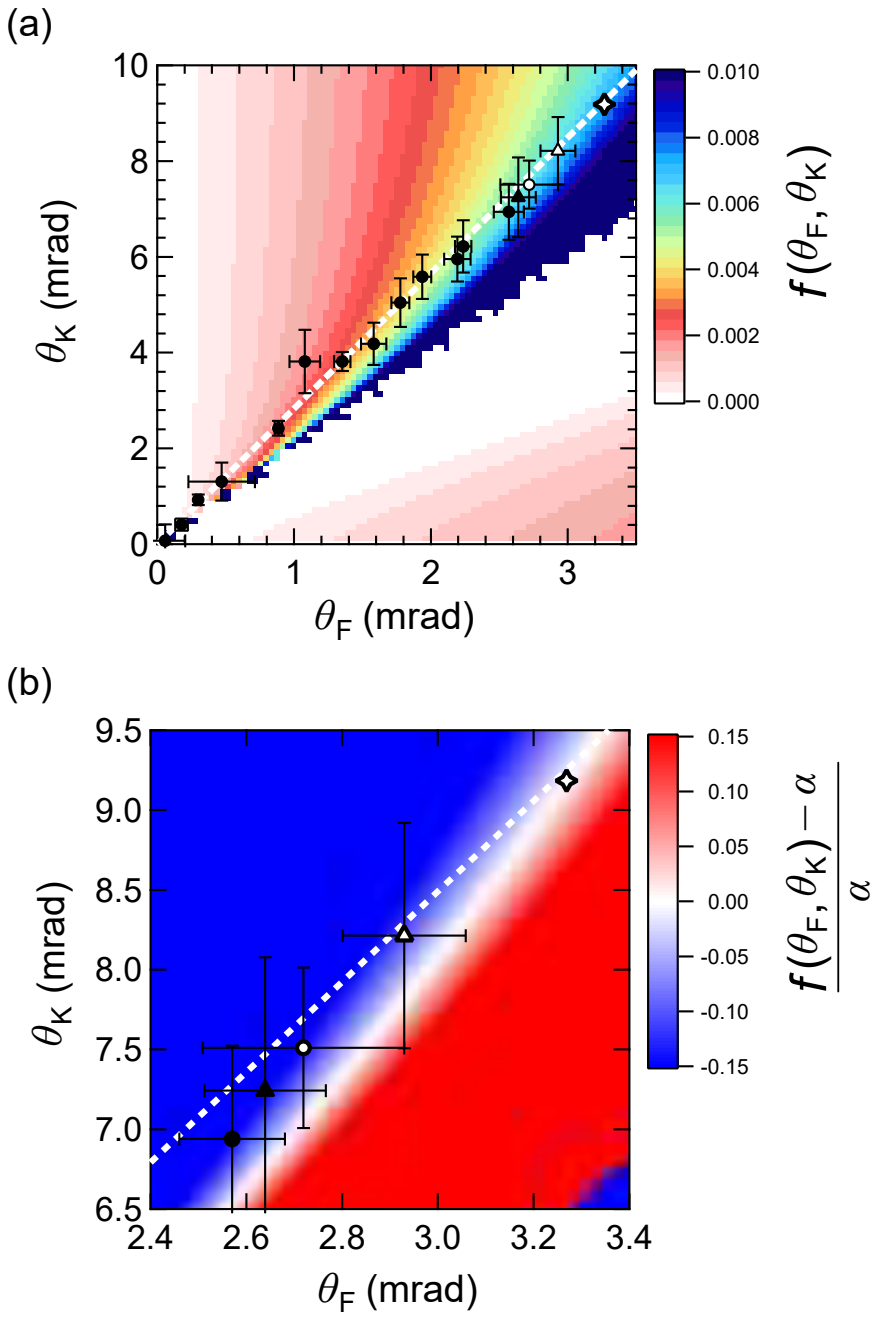

Figure 4.8: Trajectory of the Faraday (θ_F) and Kerr rotation angles (θ_K) towards the quantized values (represented by the open star), overlaid on the image plot of (a) $f(\theta_F, \theta_K)$ and (b) $\frac{f(\theta_F,\theta_K)-\alpha}{\alpha}$. α denotes the fine-structure constant. The error bars are identical to the ones presented in Figs. 4.6(b) and 4.6(c). The dashed line represents the ideal trajectory expected from Eqs. (4.9) and (4.10) in the text.

The primary cause of the reduction of the rotation angles would be residual in-gap states formed by impurities or defects. Wilson *et al.* [78] predicted that excitations from localized impurity states to the massive surface band and vice versa are magneto-optically active and resonantly modify the rotation angles (see Figs. 4.9 and the arrows in Figs. 4.9(c) and 4.9(d)). Here they assumed a single energy level for the impurity states but in our case we should take into account broad distributions of localized states within the mass gap originating from Cr impurities or Bi(Sb) defects and disorders. Then the calculated resonant features would turn into much more smeared ones. We note that in the quantum Hall regime optical probes are far more sensitive to those impurities than transport measurements; the former directly detects the conductance of the surface states averaged over the shined area, while the latter detects the chiral edge conduction developing at the edge of the sample, rather independently on impurities or defects inside the sample. This would lead to the reductions of the measured rotation angles from the ideal values expected from the almost completely-quantized $\sigma_{xy}^{\mathrm{d.c.}}$ (Figs. 4.2(c) and 4.2(d)).

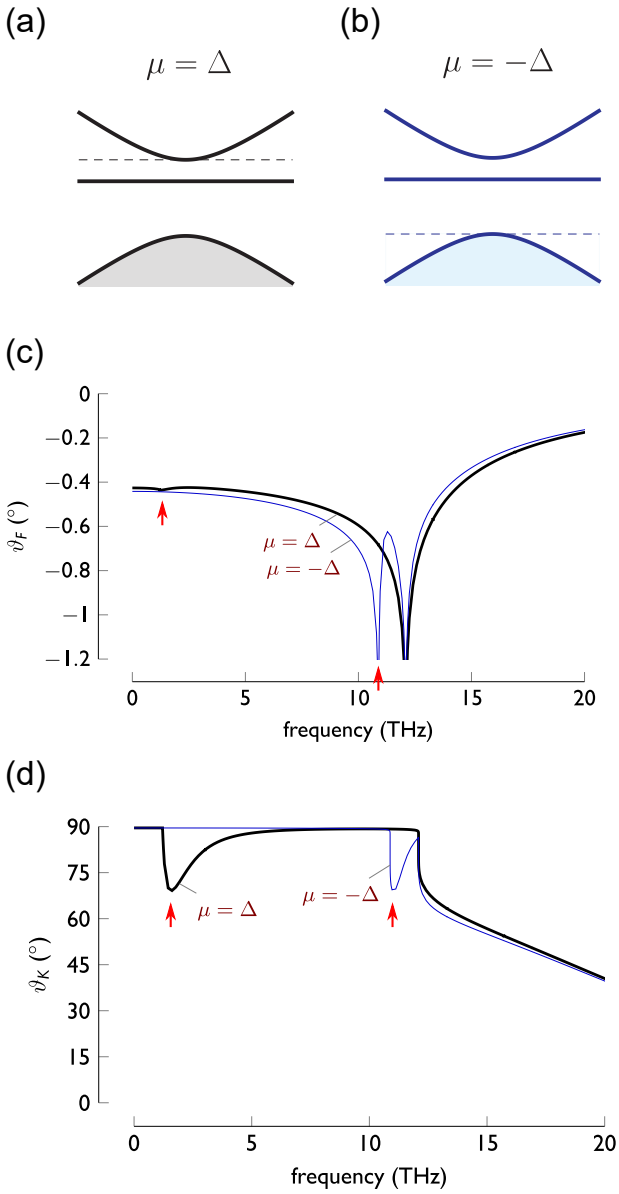

Figure 4.9: Impurity effects on magneto-optical spectra on a free-standing slab of magnetic TI [78]. (a), (b) Schematic diagrams of the energy dispersions of the massive Dirac surface states, together with the energy levels of localized states. For (a) and (b), the chemical potential (μ) coincides with Δ and $-\Delta$, measured from the Dirac point (Δ: half the size of the mass gap). (c), (d) Faraday and Kerr rotation angle spectra for typical values of impurity density and coupling strength. The arrows indicate the resonance frequency in which transitions between the localized states and the surface band occur. The figures are adapted and modified from Ref. [78].

4.5 Summary

In this Chapter we investigated magneto-optical effect on magnetic TI thin films by means of THz-TDS. As a result, at the lowest temperature we observed magneto-optical Faraday and Kerr rotations quantitatively consistent with QAH effect observed in the d.c. limit. We also confirmed that those magneto-optical rotation angles approximately satisfy the universal equation characterized with the fine-structure constant α.

Appendix

Quantized magneto-optical effect on another sample with a different heterostructure

We confirmed the quantized magneto-optical effect on another thin film with a similar but different type of magnetic modulation-doping (Fig. 4.10(a)). Below we name this film as Sample B, while name the film presented in the main text as Sample A. In Figs. 4.10(b)–(d) we summarize the transport and optical characteristics for Sample B. The sample shows a ferromagnetic transition around 40 K with the onset of σ_{xy} and turns into the QAH regime as the Hall angle (σ_{xy}/σ_{xx}) exceeds 1 below 6 K (Fig. 4.10(b)). Note that the ferromagnetic transition temperature $T_{\rm C}$ ($\sim$ 40 K) is substantially suppressed compared with Sample A ($T_{\rm C} \sim$ 70 K). Like Sample A, the rotation angle spectra are flat with good agreement with the expected d.c. values (denoted as closed squares on the ordinates in Figs. 4.10(c) and 4.10(d)) and the ellipticity spectra are almost zero (Figs. 4.10(c) and 4.10(d)).

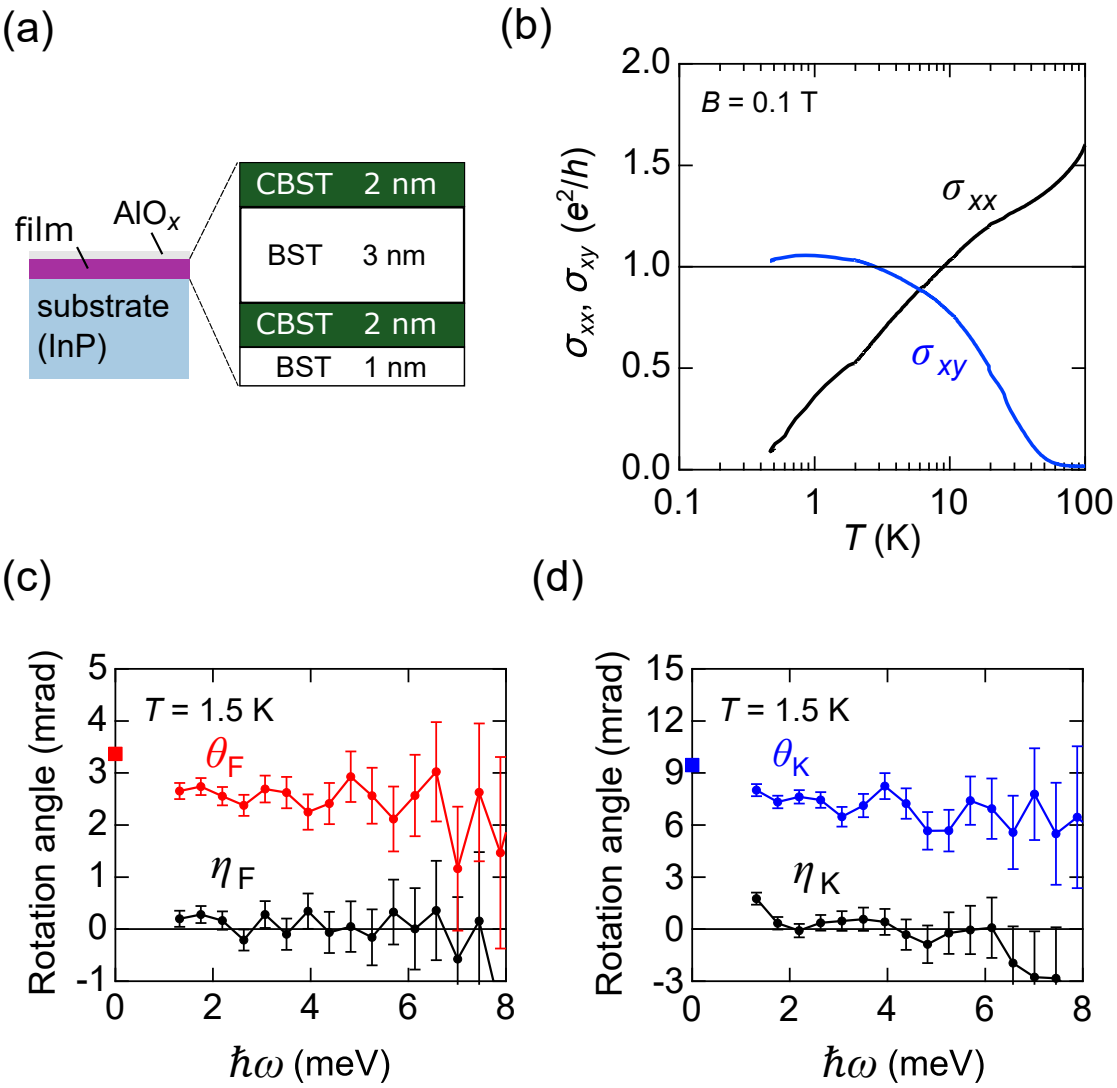

Figure 4.10: Summary of the characteristics for Sample B. (a) Schematic structure of the thin film with magnetic modulation-doping. (b) Temperature dependence of σ_{xx} and σ_{xy} at $B = 0.1$ T. (c, d) The rotation angle ($\theta_{\rm F}$, $\theta_{\rm K}$) and ellipticity ($\eta_{\rm F}$, $\eta_{\rm K}$) spectra for Faraday (c) and Kerr (d) rotations for zero magnetic field at $T = 1.5$ K. The error bars are evaluated by s.e.m. of several runs of measurement.

Quantized magneto-optical effect under magnetic field

For $B = 1$ T we performed magneto-optical measurement at $T = 1.5$ K. In Figs. 4.11 (a) and 4.11 (b) we show the Faraday and Kerr rotation spectra for Sample A, together with those under $B = 0$ T. Both are consistent with the d.c. values, denoted as open (1 T) and closed (0 T) squares on the ordinates in Figs. 4.11. As stated in the main text, the averages of the rotation angles below 4 meV are slightly higher for $B = 1$ T than those for $B = 0$ T (Figs. 4.11), probably due to the total absence of the reversal of ferromagnetic moment. Note that the Faraday rotation of the substrate (InP) is smaller than the sensitivity of our equipment (< 10 μrad T^{-1}).

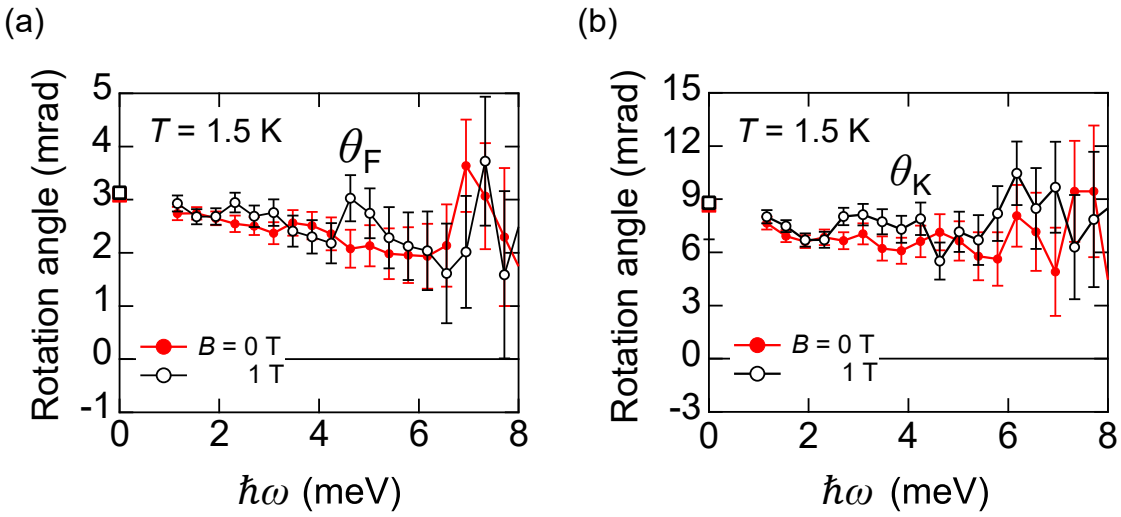

Figure 4.11: (a) Faraday ($\theta_{\rm F}$) and (b) Kerr ($\theta_{\rm K}$) rotation angle spectra at $T = 1.5$ K and $B = 0, 1$ T for Sample A. The error bars are evaluated by s.e.m. of several runs of measurement.

Chapter 5

Conclusion

In the final chapter we summarize the results obtained in this thesis and state their significance and implications. Finally, we mention future perspectives. As mentioned in Sec. 1.4, the purpose of this thesis was to explore novel optical properties of the surface Dirac electron states on topological insulator (TI), focusing on spin-polarized photocurrent, i.e., circular photogalvanic (CPG) current in the formal terminology, and magneto-optical effect on magnetic TI.

In Chap. 3 we achieved efficient generation of CPG current through careful optimization of the Fermi energy. We found that CPG current is steeply enhanced when the Fermi energy is located within the bulk band gap, due presumably to suppressed scattering of photo-excited surface Dirac electrons to the bulk states. The maximum generation efficiency of the CPG effect obtained in our experiment reaches a substantially large value comparable to those of semiconductor quantum wells.

In Chap. 4 we observed quantization of magneto-optical effect under zero magnetic field on quantum anomalous Hall (QAH) states emergent on magnetic TI samples. In the quantum limit, as theoretically predicted, the Faraday and Kerr rotations are correlated with each other in a universal relation defined by the fine-structure constant α ($= e^2/4\pi\epsilon_0\hbar c \sim 1/137$), irrespective of material parameters such as dielectric constant or thickness of the film and substrate. This universality ensures that the quantization of magneto-optical rotation angles observed here is a quantum phenomenon, along with the Hall conductance quantization in quantum

(anomalous) Hall insulators or flux quantization in superconductors.

Thus, we have uncovered novel optical responses in TI through the demonstration of the enlarged CPG current and quantized magneto-optical effect. Those achievements not only deepen the understanding of electromagnetic responses in TI but also signify notable importance of TI in both aspects of application and fundamental physics.

In the future a number of intriguing optical phenomena and functionalities in TI await for experimental demonstration including optical spin-transfer torque [79], topological magnetoelectric responses [80–83] and photo-induced quantum Hall effect [84]. Moreover, there have been an increasing number of interesting predictions [85–87] and experiments [88, 89] on optical phenomena in recently-discovered Weyl semimetals [90], which host bulk Weyl electrons that can be regarded as the three-dimensional analogue of the surface states of TI. We believe that our demonstrations of novel optical responses in TI will stimulate researchers towards those exciting and challenging phenomena and contribute to the expanding research field of electromagnetic responses of Weyl electron systems.

References

[1] M. V. Berry, Proceedings of the Royal Society of London. Series A, Mathematical and Physical Sciences **392**, 45 (1984).

[2] M. Z. Hasan and C. L. Kane, Rev. Mod. Phys. **82,** 3045 (2010).

[3] D. Thouless, M. Kohmoto, M. Nightingale, and M. den Nijs, Phys. Rev. Lett. **49,** 405 (1982).

[4] C. L. Kane and E. J. Mele, Phys. Rev. Lett. **95,** 146802 (2005).

[5] C. L. Kane and E. J. Mele, Phys. Rev. Lett. **95,** 226801 (2005).

[6] J. Moore and L. Balents, Phys. Rev. B **75,** 121306 (2007).

[7] L. Fu, C. L. Kane, and E. Mele, Phys. Rev. Lett. **98,** 106803 (2007).

[8] X.-L. Qi and S.-C. Zhang, Rev. Mod. Phys. **83,** 1057 (2011).

[9] K. S. Novoselov, A. K. Geim, S. V Morozov, D. Jiang, M. I. Katsnelson, I. V Grigorieva, S. V Dubonos, and A. A. Firsov, Nature **438,** 197 (2005).

[10] Y. Zhang, Y. Tan, H. L. Stormer, and P. Kim, Nature **438,** 201 (2005).

[11] L. Fu and C. L. Kane, Phys. Rev. B **76,** 045302 (2007).

[12] B. A. Bernevig, T. L. Hughes, and S.-C. Zhang, Science **314,** 1757 (2006).

[13] M. Konig, S. Wiedmann, C. Brune, A. Roth, H. Buhmann, L. W. Molenkamp, X.-L. Qi, and S. Zhang, Science **318,** 766 (2007).

[14] Y. Ando, J. Phys. Soc. Japan, **82,** 102001 (2013).

[15] H. Zhang, C. Liu, X. Qi, X. Dai, Z. Fang, and S.-C. Zhang, Nat. Phys. **5**, 438 (2009).

[16] Y. L. Chen, J. G. Analytis, J.-H. Chu, Z. K. Liu, S.-K. Mo, X. L. Qi, H. J. Zhang, D. H. Lu, X. Dai, Z. Fang, S. C. Zhang, I. R. Fisher, Z. Hussain, and Z.-X. Shen, Science **325,** 178 (2009).

[17] D. Hsieh, Y. Xia, D. Qian, L. Wray, J. H. Dil, F. Meier, J. Osterwalder, L. Patthey, J. G. Checkelsky, N. P. Ong, A. V. Fedorov, H. Lin, A. Bansil, D. Grauer, Y. S. Hor, R. J. Cava, and M. Z. Hasan, Nature **460,** 1101 (2009).

[18] Y. Xia, D. Qian, D. Hsieh, L. Wray, A. Pal, H. Lin, A. Bansil, D. Grauer, Y. S. Hor, R. J. Cava, and M. Z. Hasan, Nat. Phys. **5,** 398 (2009).

[19] J. Zhang, C.-Z. Chang, Z. Zhang, J. Wen, X. Feng, K. Li, M. Liu, K. He, L. Wang, X. Chen, Q.-K. Xue, X. Ma, and Y. Wang, Nat. Commun. **2,** 574 (2011).

[20] R. Yoshimi, A. Tsukazaki, Y. Kozuka, J. Falson, K. S. Takahashi, J. G. Checkelsky, N. Nagaosa, M. Kawasaki, and Y. Tokura, Nat. Commun. **6,** 6627 (2015).

[21] C.-Z. Chang, J. Zhang, X. Feng, J. Shen, Z. Zhang, M. Guo, K. Li, Y. Ou, P. Wei, L.-L. Wang, Z.-Q. Ji, Y. Feng, S. Ji, X. Chen, J. Jia, X. Dai, Z. Fang, S.-C. Zhang, K. He, Y. Wang, L. Lu, X.-C. Ma, and Q.-K. Xue, Science **340,** 167 (2013).

[22] J. G. Checkelsky, R. Yoshimi, A. Tsukazaki, K. S. Takahashi, Y. Kozuka, J. Falson, M. Kawasaki, and Y. Tokura, Nat. Phys. **10,** 731 (2014).

[23] X. Kou, S.-T. Guo, F. Yabin, L. Pan, M. Lang, Y. Jiang, Q. Shao, T. Nie, K. Murata, J. Tang, Y. Wang, L. He, T.-K. Lee, W.-L. Lee, and K. L. Wang, Phys. Rev. Lett. **113,** 137201 (2014).

[24] C.-Z. Chang, W. Zhao, D. Y. Kim, H. Zhang, B. A. Assaf, D. Heiman, S.-C. Zhang, C. Liu, M. H. W. Chan, and J. S. Moodera, Nat. Mater. **14,** 473 (2015).

[25] A. Kandala, A. Richardella, S. Kempinger, C.-X. Liu and N. Samarth, Nat. Commun. **6,** 7434 (2015).

[26] M. Mogi, R. Yoshimi, A. Tsukazaki, K. Yasuda, Y. Kozuka, K. S. Takahashi, M. Kawasaki, and Y. Tokura, Appl. Phys. Lett. **107,** 182401 (2015).

[27] R. Yoshimi, K. Yasuda, A. Tsukazaki, K. S. Takahashi, N. Nagaosa, M. Kawasaki, and Y. Tokura, Nat. Commun. **6,** 8530 (2015).

[28] A. R. Mellnik, J. S. Lee, A. Richardella, J. L. Grab, P. J. Mintun, M. H. Fischer, A. Vaezi, A. Manchon, E.-A. Kim, N. Samarth, and D. C. Ralph, Nature **511,** 449 (2014).

[29] Y. Shiomi, K. Nomura, Y. Kajiwara, K. Eto, M. Novak, K. Segawa, Y. Ando, and E. Saitoh, Phys. Rev. Lett. **113,** 196601 (2014).

[30] Y. Fan, P. Upadhyaya, X. Kou, M. Lang, S. Takei, Z. Wang, J. Tang, L. He, L.-T. Chang, M. Montazeri, G. Yu, W. Jiang, T. Nie, R. N. Schwartz, Y. Tserkovnyak, and K. L. Wang, Nat. Mater. **13,** 699 (2014).

[31] C. H. Li, O. M. J. van 't Erve, J. T. Robinson, Y. Liu, L. Li, and B. T. Jonker, Nat. Nanotechnol. **9,** 218 (2014).

[32] K. Kondou, R. Yoshimi, A. Tsukazaki, Y. Fukuma, J. Matsuno, K. S. Takahashi, M. Kawasaki, Y. Tokura, and Y. Otani, Nat. Phys. **12,** 1027 (2016).

[33] V. M. Edelstein, Solid State Commun. **73,** 233 (1990).

[34] K. v. Klitzing, G. Dorda, and M. Pepper, Phys. Rev. Lett. **45,** 494 (1980).

[35] R. Laughlin, Phys. Rev. B **23,** 5632 (1981).

[36] B. Halperin, Phys. Rev. B **25,** 2185 (1982).

[37] Y. Xu, I. Miotkowski, C. Liu, J. Tian, H. Nam, N. Alidoust, J. Hu, C.-K. Shih, M. Z. Hasan, and Y. P. Chen, Nat. Phys. **10,** 23 (2014).

[38] F. D. Haldane, Phys. Rev. Lett. **61,** 2015 (1988).

[39] K. Ohgushi, S. Murakami, and N. Nagaosa, Phys. Rev. B **62,** R6065 (2000).

[40] N. Nagaosa, J. Sinova, S. Onoda, A. H. MacDonald, and N. P. Ong, Rev. Mod. Phys. **82,** 1539 (2010).

[41] X.-L. Qi, Y.-S. Wu, and S.-C. Zhang, Phys. Rev. B **74,** 085308 (2006).

[42] R. Yu, W. Zhang, H. J. Zhang, S.-C. Zhang, X. Dai, and Z. Fang, Science **329,** 61 (2010).

[43] J. W. McIver, D. Hsieh, H. Steinberg, P. Jarillo-Herrero, and N. Gedik, Nat. Nanotechnol. **7,** 96 (2012).

[44] J. Duan, N. Tang, X. He, Y. Yan, S. Zhang, X. Qin, X. Wang, X. Yang, F. Xu, Y. Chen, W. Ge, and B. Shen, Sci. Rep. **4,** 4889 (2014).

[45] C. Kastl, C. Karnetzky, H. Karl, and A. W. Holleitner, Nat. Commun. **6,** 6617 (2015).

[46] J. N. Hancock, J. L. M. van Mechelen, A. B. Kuzmenko, D. van der Marel, C. Brune, E. G. Novik, G. V. Astakhov, H. Buhmann, and L. W. Molenkamp, Phys. Rev. Lett. **107,** 136803 (2011).

[47] A. M. Shuvaev, G. V. Astakhov, G. Tkachov, C. Brune, H. Buhmann, L. W. Molenkamp, and A. Pimenov, Phys. Rev. B **87,** 121104(R) (2013).

[48] R. Valdes Aguilar, A. V. Stier, W. Liu, L. S. Bilbro, D. K. George, N. Bansal, L. Wu, J. Cerne, A. G. Markelz, S. Oh, and N. P. Armitage, Phys. Rev. Lett. **108,** 087403 (2012).

[49] L. Wu, W.-K. Tse, M. Brahlek, C. M. Morris, R. Valdes Aguilar, N. Koirala, S. Oh, and N. P. Armitage, Phys. Rev. Lett. **115,** 217602 (2015).

[50] G. S. Jenkins, A. B. Sushkov, D. C. Schmadel, N. P. Butch, P. Syers, J. Paglione, and H. D. Drew, Phys. Rev. B **82,** 125120 (2010).

[51] G. S. Jenkins, A. B. Sushkov, D. C. Schmadel, M.-H. Kim, M. Brahlek, N. Bansal, S. Oh, and H. D. Drew, Phys. Rev. B **86,** 235133 (2012).

[52] A. A. Schafgans, K. W. Post, A. A. Taskin, Y. Ando, X.-L. Qi, B. C. Chapler, and D. N Basov, Phys. Rev. B **85,** 195440 (2012).

[53] R. Yoshimi, A. Tsukazaki, K. Kikutake, J. G. Checkelsky, K. S. Takahashi, M. Kawasaki, and Y. Tokura, Nat. Mater. **13,** 253 (2014).

[54] S. D. Ganichev, and W. Prettl, J. Phys. Condens. Matter. **15,** R935 (2003).

[55] N. Ogawa, M. S. Bahramy, Y. Kaneko, and Y. Tokura, Phys. Rev. B **90,** 125122 (2014).

[56] H. Yuan, X. Wang, B. Lian, H. Zhang, X. Fang, B. Shen, G. Xu, Y. Xu, S.-C. Zhang, H. Y. Hwang, and Y. Cui, Nat. Nanotechnol. **9,** 851 (2014).

[57] M. Eginligil, B. Cao, Z. Wang, X. Shen, C. Cong, J. Shang, C. Soci, and T. Yu, Nat. Commun. **6,** 7636 (2015).

[58] F. Meier and B. P. Zakharchenya, Optical Orientation (Elsevier, Amsterdam, 1984).

[59] P. Olbrich, L. E. Golub, T. Herrmann, S. N. Danilov, H. Plank, V. V. Bel'kov, G. Mussler, Ch. Weyrich, C. M. Schneider, J. Kampmeier, D. Grutzmacher, L. Plucinski, M. Eschbach, and S. D. Ganichev, Phys. Rev. Lett. **113,** 096601 (2014).

[60] B. Yu. Yavorsky, N. F. Hinsche, I. Mertig, and P. Zahn, Phys. Rev. B **84,** 165208 (2011).

[61] G. Wang and T. Cagin, Phys. Rev. B **76,** 075201 (2007).

[62] A. A. Reijnders, Y. Tian, L. J. Sandilands, G. Pohl, I. D. Kivlichan, S. Y. Frank Zhao, S. Jia, M. E. Charles, R. J. Cava, N. Alidoust, S. Xu, M. Neupane, M. Z. Hasan, X.Wang, S. W. Cheong, and K. S. Burch, Phys. Rev. B **89,** 075138 (2014).

[63] X. Zhu, L. Santos, C. Howard, R. Sankar, F. C. Chou, C. Chamon, and M. El-Batanouny, Phys. Rev. Lett. **108,** 185501 (2012).

[64] C. Chen, Z. Xie, Y. Feng, H. Yi, A. Liang, S. He, D. Mou, J. He, Y. Peng, X. Liu, Y. Liu, L. Zhao, G. Liu, X. Dong, J. Zhang, L. Yu, X. Wang, Q. Peng, Z. Wang, S. Zhang, F. Yang, C. Chen, Z. Xu, and X. J. Zhou, Sci. Rep. **3,** 2411 (2013).

[65] Y. H. Wang, D. Hsieh, E. J. Sie, H. Steinberg, D. R. Gardner, Y. S. Lee, P. Jarillo-Herrero, and N. Gedik, Phys. Rev. Lett. **109,** 127401 (2012).

[66] D. Niesner, Th. Fauster, S. V. Eremeev, T. V. Menshchikova, Yu. M. Koroteev, A. P. Protogenov, E. V. Chulkov, O. E. Tereshchenko, K. A. Kokh, O. Alekperov, A. Nadjafov, and N. Mamedov, Phys. Rev. B **86,** 205403 (2012).

[67] J. S. Lee, A. Richardella, D. R. Hickey, K. A. Mkhoyan, and N. Samarth, Phys. Rev. B **92,** 155312 (2015).

[68] S. D. Ganichev, E. L. Ivchenko, S. N. Danilov, J. Eroms, W. Wegscheider, D. Weiss, and W. Prettl, Phys. Rev. Lett. **86,** 4358 (2001).

[69] S. D. Ganichev, U. Rössler, W. Prettl, E. L. Ivchenko, V. V. Bel'kov, R. Neumann, K. Brunner, and G. Abstreiter, Phys. Rev. B **66,** 075328 (2002).

[70] W.-K. Tse and A. H. MacDonald, Phys. Rev. Lett. **105,** 057401 (2010).

[71] J. Maciejko, X.-L. Qi, H. D. Drew, and S.-C. Zhang, Phys. Rev. Lett. **105,** 166803 (2010).

[72] Y. Jiang, C. Song, Z. Li, M. Chen, R. L. Greene, K. He, L. Wang, X. Chen, X. Ma, and Q.-K. Xue, Phys. Rev. B **92,** 195418 (2015).

[73] I. Lee, C. K. Kim, J. Lee, S. J. L. Billinge, R. Zhong, J. A. Schneeloch, T. Liu, T. Valla, J. M. Tranquada, G. Gu, and J. C. Seamus Davis, Proc. Natl. Acad. Sci. USA **112,** 1316 (2015).

[74] R. Shimano, G. Yumoto, J. Y. Yoo, R. Matsunaga, S. Tanabe, H. Hibino, T. Morimoto, and H. Aoki, Nat. Commun. **4,** 1841 (2013).

[75] K. W. Post, B. C. Chapler, M. K. Liu, J. S. Wu, H. T. Stinson, M. D. Goldflam, A. R. Richardella, J. S. Lee, A. A. Reijnders, K. S. Burch, M. M. Fogler, N. Samarth, and D. N. Basov, Phys. Rev. Lett. **115,** 116804 (2015).

[76] L. I. Berger, Semiconductor Materials (CRC Press, 1996).

[77] M. Kucera, S. Visnovsky, and V. Prosser, IEEE Transactions on Magnetics **20,** 989 (1984).

[78] J. H. Wilson, D. K. Efimkin, and V. M. Galitski, Phys. Rev. B **90,** 205432 (2014).

[79] P. Năemec, E. Rozkotová, N. Tesařová, F. Trojánek, E. De Ranieri, K. Olejník, J. Zemen, V. Novák, M. Cukr, P. Malý, and T. Jungwirth, Nat. Phys. **8,** 411 (2012).

[80] X.-L. Qi, R. Li, J. Zang, and S.-C. Zhang, Science **323,** 1184 (2009).

[81] T. Morimoto, A. Furusaki, and N. Nagaosa, Phys. Rev. B **92,** 085113 (2015).

[82] J. Wang, B. Lian, X.-L. Qi, and S.-C. Zhang, Phys. Rev. B **92,** 081107 (2015).

[83] M. Mogi, M. Kawamura, R. Yoshimi, A. Tsukazaki, Y. Kozuka, N. Shirakawa, K. S. Takahashi, M. Kawasaki, and Y. Tokura, Nat. Mater. **16,** 516 (2017).

[84] Y. H. Wang, H. Steinberg, P. Jarillo-Herrero, and N. Gedik, Science **342,** 453 (2013).

[85] K. Taguchi, T. Imaeda, M. Sato, and Y. Tanaka, Phys. Rev. B **93,** 201202(R) (2016).

[86] C.-K. Chan, N. H. Lindner, G. Refael, and P. A. Lee, Phys. Rev. B **95,** 041104 (2017).

[87] P. Goswami, G. Sharma, and S. Tewari, Phys. Rev. B **92,** 161110(R) (2015).

[88] L. Wu, S. Patankar, T. Morimoto, N. L. Nair, E. Thewalt, A. Little, J. G. Analytis, J. E. Moore, and J. Orenstein, Nat. Phys. **13,** 350 (2017).

[89] Q. Ma, S.-Y. Xu, C.-K. Chan, C.-L. Zhang, G. Chang, Y. Lin, W. Xie, T. Palacios, H. Lin, S. Jia, P. A. Lee, P. Jarillo-Herrero, and N. Gedik, Nat. Phys. doi:10.1038/nphys4146 (2017).

[90] B. Yan and C. Felser, Annu. Rev. Cond. Mat. Phys. **8,** 337 (2017).

Publication list

1. K. N. Okada, N. Ogawa, R. Yoshimi, A. Tsukazaki, K. S. Takahashi, M. Kawasaki, and Y. Tokura

   "Enhanced photogalvanic current in topological insulators via Fermi energy tuning"

   Phys. Rev. B **93,** 081403(R) (2016).

2. K. N. Okada, Y. Takahashi, M. Mogi, R. Yoshimi, A. Tsukazaki, K. S. Takahashi, N. Ogawa, M. Kawasaki, and Y. Tokura

   "Terahertz spectroscopy on Faraday and Kerr rotations in a quantum anomalous Hall state"

   Nat. Commun. **7,** 12245 (2016).

Acknowledgement

First and foremost, I would like to express my sincere gratitude to Prof. Yoshinori Tokura for his supervision for totally five years and a half since the final year of my bachelor course. His attitude towards exploring new physics has made a great impact on me and continuously served as a model of physicist.

I would also like to show my special appreciation to Prof. Yukitoshi Motome for kindly giving me an opportunity for theoretical studies for the latter half of my doctoral course.

This thesis would not have been possible without collaborations with the following people. I am particularly indebted to Dr. Naoki Ogawa for guidance in photocurrent measurement, Prof. Youtarou Takahashi for instruction in terahertz spectroscopy and Dr. Ryutaro Yoshimi for many supports and advices on thin film growth and device fabrications. I would like to appreciate valuable suggestions on thin film growth from Prof. Masashi Kawasaki, Prof. Atsushi Tsukazaki and Dr. Kei S. Takahashi. I also thank Mr. Masataka Mogi for providing me high-quality samples.

I am grateful to all my collegues in Tokura group and the members in RIKEN CEMS for stimulating discussions and assistance in experiment.

I would be grateful to the referees of the thesis defense, Prof. Yoshihiro Iwasa, Prof. Yukitoshi Motome, Prof. Kyoko Ishizaka and Dr. Naoki Ogawa for giving me valuable comments and reviewing this thesis.

Finally, I feel deeply thankful to my parents for the enormous and continuous support during my graduate study.